Saturn's F Ring core: Calm in the midst of chaos

J. N. Cuzzi[*,a], A. D. Whizin[b], R. C. Hogan[c], A. R. Dobrovolskis[d], L. Dones[e], M. R. Showalter[f], J. E. Colwell[b], and J. D. Scargle[a]

April 29, 2013

Abstract

The long-term stability of the narrow F Ring core has been hard to understand. Instead of acting as "shepherds", Prometheus and Pandora together stir the vast preponderance of the region into a chaotic state, consistent with the orbits of newly discovered objects like S/2004S6. We show how a comb of very narrow radial locations of high stability in semimajor axis is embedded within this otherwise chaotic region. The stability of these semimajor axes relies fundamentally on the unusual combination of rapid apse precession and long synodic period which characterizes the region. This situation allows stable "antiresonances" to fall on or very close to traditional Lindblad resonances which, under more common circumstances, are destabilizing. We present numerical integrations of tens of thousands of test particles over tens of thousands of Prometheus orbits that map out the effect. The stable antiresonance zones are *most* stable in a subset of the region where Prometheus first-order resonances are least cluttered by Pandora resonances. This region of optimum stability is paradoxically closer to Prometheus than a location more representative of "torque balance", helping explain a longstanding paradox. One stable zone corresponds closely to the currently observed semimajor axis of the F Ring core. While the model helps explain the stability of the narrow F Ring core, it does not explain why the F Ring material all shares a common apse longitude; we speculate that collisional damping at the preferred semimajor axis (not included in the current simulations) may provide that final step. Essentially, we find that the F Ring core is not confined by a combination of Prometheus and Pandora, but a combination of Prometheus and precession.

(*) Corresponding Author; Mail Stop 245-3; 650-604-6343
(a) Space Science Division, Ames Research Center, NASA; Moffett Field CA 94035
(b) Department of Physics, University of Central Florida, Orlando FL
(c) BAERI, inc. Sonoma, CA (deceased)
(d) Astronomy Department, University of California, Santa Cruz, CA; currently at (e)
(e) SETI Institute; Mountain View CA
(f) SWRI, inc. Boulder, CO

Authors' email addresses: jeffrey.cuzzi@nasa.gov; awhizin@yahoo.com; anthony.r.dobrovolskis@nasa.gov; luke@boulder.swri.edu; mshowalter@seti.org; jec@ucf.edu; jeffrey.d.scargle@nasa.gov

Keywords: Planetary Rings; Saturn, Rings; Resonances, Rings; Resonances, orbital; Celestial Mechanics. Note "Resonances" in the online Keywords list is mis-spelled "Reasonances" in two places.

1 Introduction

Saturn's "kinky" F Ring has attributes which depend on the observing geometry and wavelength. Imaging observations best reveal its dramatic, spiky longitudinal structure, which depends on both time and longitude relative to Prometheus. The so-called "gap and streamer" structure has been explained by Prometheus perturbations (Murray et al. 2005, 2008; Chavez 2009; Beurle et al. 2010). Evanescent outlier strands of a spiral nature, usually present and extending to hundreds of km from the core, are thought to result from ongoing collisions with crossing bodies (Charnoz et al. 2005). Images show that much of the F Ring particle area is in particles smaller than 100 μm (Showalter et al. 1992) with globally time-variable abundance (French et al. 2012). However, the spiky structure, "fans", and "mini-jets" (Beurle et al. 2010, Attree et al. 2012) also require some large but countable number of embedded bodies of sizes perhaps up to a km or so. Stellar occultations are, like the images, sensitive to particles larger than about a micron. They show the ring to have a narrow core with width of order 10 km, and reveal sporadic off-core clumpiness (Albers et al. 2012, Meinke et al. 2012). Radio occultations from Cassini and Voyager (sensitive to cm and larger size particles) reveal what must be the true core of the ring to be only about 100 meters wide, and azimuthally broken so that it is only seen on one-third of radio occultations (Marouf et al. 2011).

Application to the F Ring of the original "shepherding" concept (*eg.* Goldreich and Tremaine 1979) has a problem, in that the ring is not in torque balance between the putative shepherds (Showalter and Burns 1982; henceforth SB82). However, when resonances are not overlapping, the ring could in principle find its support from an isolated resonance in some way, without being "in balance" between the two straddling ringmoons (see section 4); what we will propose is in fact somewhat along these lines. Indeed the F Ring region is filled with a comb of resonances (**figure 1**). Because of the sizeable eccentricities of Prometheus and Pandora, second- (and higher-) order resonances have significant strength, especially close to the moons.

Noting the puzzle of the F Ring location and stability, Cuzzi and Burns (1988; CB88) suggested that the F Ring is not shepherded, but is only one of a series of transitory features arising from collisions between multiple km-size moonlets in a moonlet belt lying between Prometheus and Pandora. Scargle et al. (1993), in a preliminary version of the work presented here, presented a simple toy model for cyclic eccentricity variations, and orbital integrations showing large eccentricity fluctuations of objects throughout the region caused by repeated encounters with Prometheus and Pandora. They noted that the Chirikov criterion (Wisdom 1983) for the radial width of a chaotic zone (say, surrounding Prometheus or Pandora) was an underestimate. Because of the significant eccentricities of Prometheus and Pandora, higher-order resonances with closer spacings than those found for circular perturbers play a role, overlap sooner, and yield chaotic zones which are considerably wider than predicted by the Chirikov criterion. They suggested that the entire region was chaotic. Winter et al.. (2007, 2010) and Sfair et al. (2009) demonstrated this convincingly with detailed numerical integrations and analytical modeling.

Cassini has found a number of objects with plausibly chaotic properties, such as S/2004 S6 (henceforth 2004S6) and similar objects; it is hard even to get an orbit for these objects (N. Cooper, personal communication 2012) given observations spaced by months. Where do they come from? Their eccentricities (several times 10^{-3}) are much larger than assumed in the moonlet belt models of CB88, in which the ensemble eccentricities (a few times 10^{-4} at the F Ring) were assumed to be only due to single passage perturbations by Prometheus. Attree et al. (2012) postulated a comparably low eccentricity (about 10^{-4}) for objects *within* the core, in the absence of strong damping, suggesting that damping between Prometheus encounters maintained their low values. Yet, it is not clear whether the large objects presumably observed by Attree et al. (2012) can be damped so quickly by the small

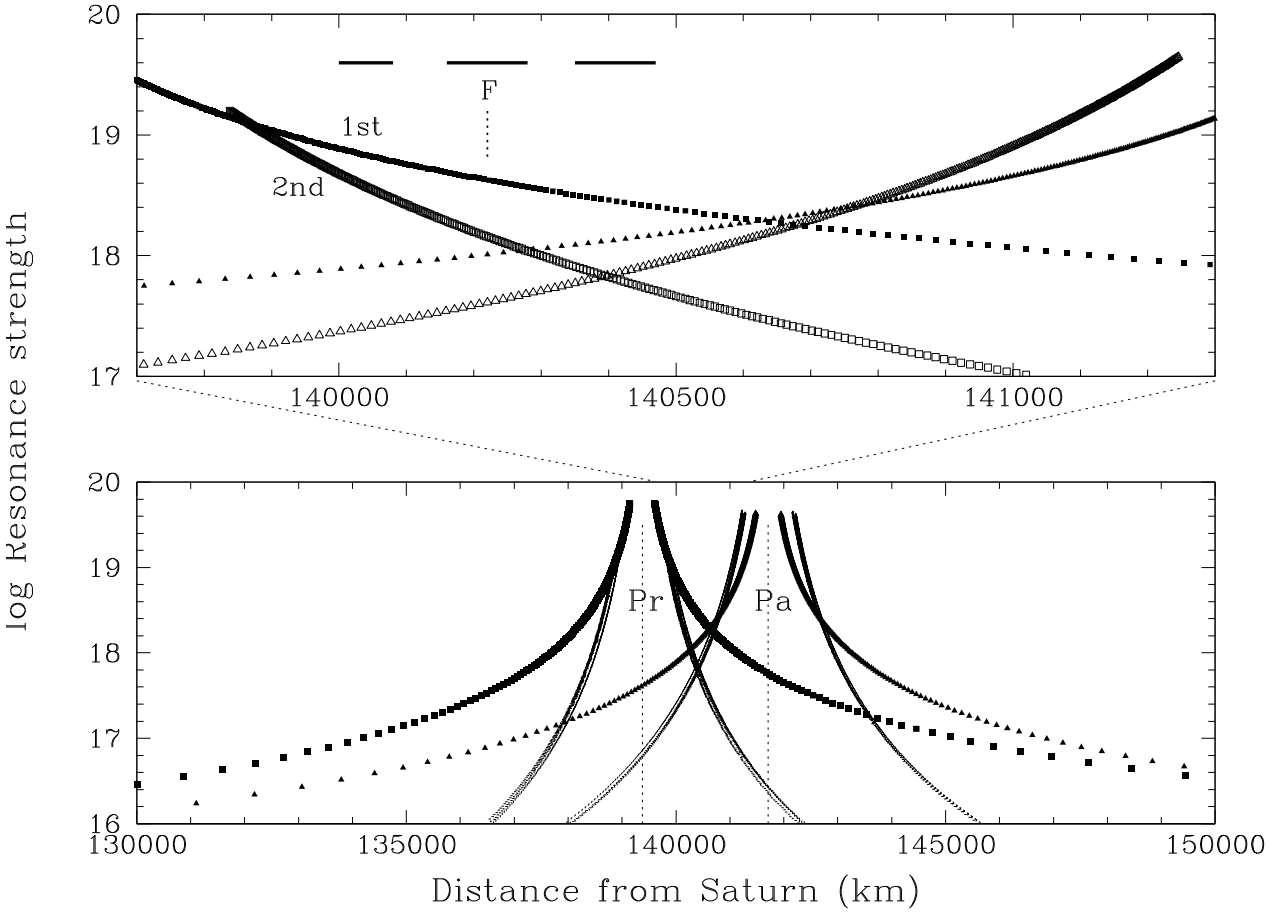

Figure 1: An overview of the region surrounding Prometheus and Pandora (the broadly-defined "F Ring region"), showing first and second order Lindblad resonances with the two so-called "shepherds" (filled and open symbols respectively). The vertical dotted line at 140220km indicates the semimajor axis of the F Ring. The heavy horizontal bars indicate the three radial regions we have studied in detail (section 3). Resonance location and strength calculations are described in Appendix A.

particles making up the bulk of the F Ring, any more than 2004S6 is, which crosses the ring routinely. On the other hand, even a grazing Prometheus passage would only confer an eccentricity of about 5×10^{-4}. How then can we explain the large observed eccentricities for 2004S6 and its kin without cumulative, chaotic effects?

The observed presence of large eccentricities, and the theoretical results of Winter et al. (2007, 2010) suggest that chaotic behavior is pervasive. Indeed 2004S6 does seem to have violent collisional interactions with the F Ring core, which it crosses regularly. In 2008, a substantial strand was torn from the F Ring core, growing to cover nearly 200 km in semimajor axis, and dispersing over a period of several years, with several apparently co-orbital clumps being its last-seen remnants (Murray et al. 2011, French et al. 2012). The very large clumps seen in the 1995-1996 ring plane crossing by McGhee et al. (2001) may be other examples of this rare phenomenon. These substantial bursts of material do not become new F Rings like the long-lived core, but disperse rapidly even while not very far away from the core.

In the presence of large perturbations even *away* from resonances, which lead to the chaotic

behavior demonstrated by Winter et al. (2007), it is hard to understand how the narrow F Ring core can be preserved at essentially the *same* semimajor axis as seen during Voyager, precessing uniformly since then (Bosh et al. 2002, Murray et al. 2011, Marouf et al. 2011, Albers et al. 2012, Cooper et al. 2012). A connected puzzle is a strangely undistorted "pencil line" strand observed occasionally by Murray et al. (2008; see also Colwell et al. 2009). How does this strand avoid incurring the ubiquitous spiky structures produced when Prometheus is near apoapse (Murray et al. 2008, 2010; Beurle et al. 2010), and how does the F Ring core remain so calm and unperturbed in the global sense? That is, if large and dispersive perturbations *are* the rule, as suggested by our models and by Winter et al. (2007, 2010), and demonstrated by the 2008 strand, how does the F core itself, which contains numerous sizeable objects in addition to μm-sized dust, maintain its very stable orbit (Bosh et al. 2002, Marouf et al. 2011, Murray et al. 2011) and low relative velocities observed by Attree et al. (2012)?

We present in this paper the first part of an explanation for at least some of these puzzles: a novel "antiresonance" in which an unusual combination of orbital properties in the region causes semimajor axis perturbations from Prometheus on successive encounters to cancel, or nearly so, *at or near traditional Lindblad resonances*. Without this special situation, which provides *prompt cancellation* of successive Prometheus perturbations, the eccentricity of the embedded core moonlet population would inevitably grow to several times 10^{-3}, as seen for 2004S6 and other discrete objects. We believe that the F Ring core lies quietly where it does because its material has found one of a number of very narrow (< 1) km locations, with the roughly 8 km spacing of Prometheus first-order resonances, which are stable to chaotic dispersion because of this prompt cancellation.

In Section 2, we describe a "toy" physical model motivating the effect. In section 3, we present extensive numerical integrations of tens of thousands of test particles, illustrating the effect. In section 4, we discuss the implications. In section 5 we present our main conclusions and note future work. In Appendices A and B we give some background on resonances and our numerical code, respectively.

2 Physical models

In this section we introduce the orbital geometry of interest and describe a toy model, that provides physical insight into our numerical results. The toy model has the nature of a "map" (Duncan et al. 1989) in that we simplify the radial and tangential accelerations on a massless (ring) particle due to a nearby perturber as impulses with strength averaged over an encounter having duration less than an orbit period, exerted at close encounters or conjunctions that occur every synodic period. For similar approaches and more background see Murray and Dermott (1999) and Showalter and Burns (1982). The orbit parameters entering into the toy model are the semimajor axis a, eccentricity e, pericenter longitude ω, mean motion n, and true anomaly f (for definitions of these standard orbital elements see Murray and Dermott (1999), Burns 1976, or Danby 1962). The toy models described here involve a single dominant perturber, but our full numerical integrations (section 3) allow for the full set of 14 gravitationally active moons, time-variable forces, and realistic orbit elements (see Appendix B).

A good physically-based derivation of the perturbation equations is given by Burns (1976), where the most relevant are[1]:

$$\frac{de}{dt} = \gamma[R\sin f + T(\cos f + \cos\xi)]$$

[1]Note typos in equations (24) and (41) of Burns 1976; compare with Murray and Dermott (1999) equation 2.165 (Burns, personal communication, 1976 and Burns 1977 Erratum).

$$\begin{aligned}\frac{d\omega}{dt} &= \frac{\gamma}{e}\left[-R\cos f + T\sin f\left(\frac{2+e\cos f}{1+e\cos f}\right)\right] \\ \frac{da}{dt} &= \frac{2a\gamma}{1-e^2}\left[eR\sin f + T(1+e\cos f)\right] \approx \frac{2}{n}\left[eR\sin f + T(1+e\cos f)\right].\end{aligned} \tag{1}$$

In equations (1) above, R and T are radial and tangential perturbing forces on the test particle per unit mass, ξ is the eccentric anomaly (which will not be needed because it lies in a negligible term), and we define $\gamma \equiv (a(1-e^2)/GM)^{1/2}$, where G is the gravitational constant and M is the planet's mass. In the equation for $d\omega/dt$ we (and SB82) have deleted a term related to the nodal precession rate, which contributes negligibly over the duration of each perturbation.

2.1 Eccentricity toy model

For small eccentricity, to avoid problems caused by small denominators, it is common to define the complex eccentricity as $\mathbf{E} = k + ih = e \cdot \exp(i\omega)$, where $h = e\sin\omega$ and $k = e\cos\omega$. Showalter and Burns (1982) convert equations (1) into time derivatives of h and k, using the chain rules $dh/dt = (\partial h/\partial e)(de/\partial t) + (\partial h/\partial\omega)(d\omega/\partial t)$ (*etc.*), and simple geometrical identities along the lines of $\cos\omega\cos f - \sin\omega\sin f = \cos(\omega+f) = \cos g$, where $g = f+\omega$ is measured from an inertial reference (we have retained physical units for greater transparency; see Burns 1976, Danby 1962, and Murray and Dermott 1999):

$$\begin{aligned}\frac{dh}{dt} &= \gamma\left[-R\cos g + T\left(\sin g + \frac{h+\sin g}{1+e\cos f}\right)\right] \\ \frac{dk}{dt} &= \gamma\left[R\sin g + T\left(\cos g + \frac{k+\cos g}{1+e\cos f}\right)\right],\end{aligned} \tag{2}$$

and da/dt is unchanged.

Previous mapping models make use of the fact that in the F Ring - Prometheus - Pandora geometry, conjunction separations $s \approx \Delta a \ll a$. The relative tangential velocity is $v_{rel} \approx as|dn_o/da| = 3n_o s/2$ where n_o is the test particle's mean motion. Then the duration of the encounter Δt (say the time over which the separation is less than twice its minimum value) is $\Delta t \approx 2s\sqrt{3}/v_{rel} \sim 2/n_o \sim P_o/\pi$ - a fraction of an orbit period P_o. The impulse approximation models the integrated changes over each encounter as $\Delta(h,k,a) = (dh/dt,\ dk/dt,\ da/dt)\Delta t$, where the derivatives are evaluated at conjunction. It is further assumed that no further perturbations occur until the next encounter after a synodic period $P_{syn} = 2\pi/|n_o - n_s|$, where n_s is the perturber's mean notion. During each encounter, the particle moves a longitudinal distance $v_{rel}\Delta t \sim 3s$ relative to the perturber. That is, the longitudinal motion during an encounter is about $1/\pi$ of the traditional longitudinal excursion between successive encounters, $3\pi s$ (Dermott 1981, Cuzzi and Scargle 1985).

In the limit where the radial eccentric oscillations are much smaller than the mean separation in semimajor axis, the near-symmetry as the test particle passes the perturber causes first-order cancellation of the tangential force, but not of the radial force, so $R \gg T$ and equations (2) can be greatly simplified. In section 2.2 below, we give a more detailed derivation which gives the regime of validity of this approximation as $ae \ll s$, which is satisfied by Pan and the Encke gap edges, but gets a little questionable in the F Ring-Prometheus regime. However, this limit captures the essence of the physics and has the simplest dependence on angular variables. In the limit $R \gg T$, equations (2) become:

$$\Delta h \approx \frac{dh}{dt}\Delta t \approx \frac{dh}{dt}\frac{P_o}{\pi} = -\frac{P_o\gamma R}{\pi}\cos(f+\omega) \tag{3}$$

$$\Delta k \approx \frac{dk}{dt}\frac{P_o}{\pi} = \frac{P_o \gamma R}{\pi}\sin(f+\omega)$$

where the radial force per unit mass at encounter is

$$R = GM_s/s^2 \tag{4}$$

and M_s is the perturber mass. The increments Δh_i at successive encounters separated by the synodic period P_{syn} are then, for instance,

$$\Delta h_i = -\frac{P_o \gamma R}{\pi}\cos(f_i+\omega_i) = -\frac{P_o \gamma R}{\pi}\cos(g_i) \tag{5}$$
$$\Delta h_{i+1} = -\frac{P_o \gamma R}{\pi}\cos(g_i + n_o P_{syn}),$$

where in the notation of SB82, the change in periapse longitude ω is combined with the change in true anomaly f, into a change in orbit longitude g which depends only on the mean motion n_o. That is, g has an inertial reference and $(\Delta h, \Delta k)$ do not depend on (h,k) themselves. This is a great simplification when $s \gg ae$.

Consider the situation near a Lindblad (outer) resonance[2] of order m, where for simplicity in the toy model here we assume $n_o \approx (m/m+1)n_s$; that is, the epicycle frequency is equal to the mean motion (a more accurate treatment is presented subsequently). For the F Ring regime of interest, $m \gg 1$. The distance s to the resonance can also be written as $n_o \approx n_s + s dn/da \approx n_s - 3sn_s/2a_s$ (for an outer resonance). Setting the two expressions for n_o equal, we get $s = 2a_s/3m$. Also, the spacing between resonances at this distance is obtained from $\Delta n(m, m+1) \approx n_s[m/(m+1) - (m-1)/m] \sim n_s/m^2$. If the resonance radial spacing is w, then we can also set $\Delta n = w dn/da = w \cdot (3n_o/2a) = w \cdot 3mn_s/2a(m+1)$. Solving for w gives $w = 2a/3m^2$ in the limit $m \gg 1$, which can also be expressed as $w = s/m$ or $w = 3s^2/2a$. For the case of the F Ring and Prometheus, $s \sim$ 850km, $a \sim$ 140000 km, $w \sim$ 8 km, and $m \sim 100$. We also get the useful relationship

$$P_{syn} = \frac{2\pi}{|n_o - n_s|} \approx \frac{2\pi}{s dn/da} \approx \frac{2\pi a_o}{s \cdot \frac{3}{2} n_o} = \frac{2a_o P_o}{3s} = P_o m. \tag{6}$$

Now consider a semimajor axis near some resonance of order m. Exactly at the resonance, the synodic period $P_{syn} = mP_o$, but at a fractional distance ϵ towards the next resonance, where $0 < \epsilon < 1$, $2a/3s = m + \epsilon$, so $P_{syn} = (m+\epsilon)P_o$. Midway between resonances, ϵ=0.5.

From equations (5) we can then write

$$\Delta h_{i+1} = -\frac{P_o \gamma R}{\pi}\cos(g_i + n_o(m+\epsilon)P_o) = -\frac{P_o \gamma R}{\pi}\cos(g_i + 2\pi m + 2\pi\epsilon) = -\frac{P_o \gamma R}{\pi}\cos(g_i + 2\pi\epsilon). \tag{7}$$

and similarly for Δk_{i+1}. Regarding h and k as components of a complex eccentricity vector **E**,

$$\Delta \mathbf{E}_i = \begin{pmatrix}\Delta k_i \\ \Delta h_i\end{pmatrix} = \frac{\gamma R P_o}{\pi}\begin{pmatrix}\sin g_i \\ -\cos g_i\end{pmatrix}; \quad \Delta \mathbf{E}_{i+1} = \frac{\gamma R P_o}{\pi}\begin{pmatrix}\sin(g_i + 2\pi\epsilon) \\ -\cos(g_i + 2\pi\epsilon)\end{pmatrix}. \tag{8}$$

That is, the vector $\Delta \mathbf{E}_{i+1}$ is just a rotation of the vector $\Delta \mathbf{E}_i$ by an angle $2\pi\epsilon$. The situation is illustrated in **figure 2a**, which shows the (k,h) plane for an initial $e_o = |\mathbf{E}_o| = 0$. At any time, the complex eccentricity **E** is the vector sum of all increments to date, giving orbital eccentricity $e = |\mathbf{E}|$ and pericenter longitude $\omega = \tan^{-1}(h/k)$. Each encounter leads to a vector impulse of

[2] see Appendix A for a brief review of the properties of resonances of interest

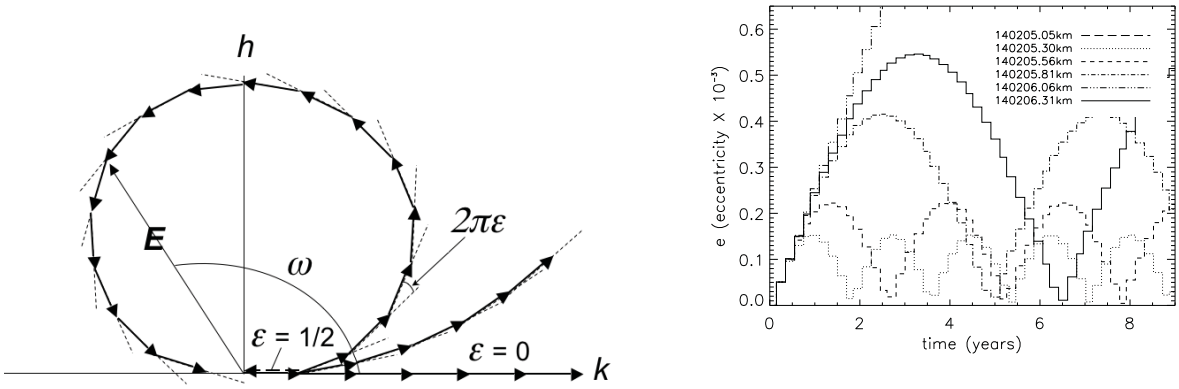

Figure 2: (a; left) The evolution of the complex eccentricity vector $\mathbf{E}$ in the (k, h) plane; $\mathbf{E}$ is the cumulative sum of individual vector perturbations at close encounters and the corresponding apse longitude ω is also indicated. In section 2.1 we show that each subsequent increment in complex eccentricity has the same amplitude but is rotated by an angle $2\pi\epsilon$ where ϵ is the fractional distance away from a Lindblad resonance. The time history of $|\mathbf{E}|$ is thus cyclic, with amplitude and period that grow as ϵ decreases. Note the small pair of opposing vectors in the case $\epsilon = 1/2$; this is the case we call prompt cancellation, in that a perturbation is immediately canceled at the next encounter, so the resultant $|\mathbf{E}|$ never gets large. (b; right) Numerical model of the time history of test particle eccentricity $|\mathbf{E}|$ in a two-body system, with a circular perturber. The individual increments occur only at conjunctions; their phased behavior causes the amplitude and period of the net eccentricity to grow as the particle's orbit approaches a resonance.

magnitude $\gamma R P_o/\pi$, which rotates from one encounter to the next by angle $2\pi\epsilon$ while a, n, and P_o are unchanged. At a resonance, where $\epsilon = 0$, each impulse adds coherently and e grows without limit (until $ae \sim s$ and P_o starts to change); see section 2.2. At various distances away from resonance, the growth of e is limited because the vector impulses eventually lead back to the origin on the timescale of $2\pi/2\pi\epsilon = 1/\epsilon$ synodic periods. The closer to resonance, the smaller is ϵ, so the number of encounters needed to return to e_o is large and $e = |\mathbf{E}|$ can attain large values, with a long period cycle. Further from resonance, ϵ increases so the cycle is faster and the periodic variation of $e = |\mathbf{E}|$ has a smaller amplitude. Exactly half way between resonances, at $\epsilon = 1/2$, the impulse vector rotates by π between successive encounters and cancels out the previous impulse, so e hardly grows at all and only jitters slightly every encounter. For lack of another term we call these locations where $\epsilon = 1/2$ *antiresonances*; at these locations *prompt cancellation* occurs of the immediately previous perturbation. Behavior like this is observed in numerical integrations involving a single perturber and a fine comb of test particles (**figure 2b**). We note again that this "map" is free of complications regarding the associated perturbations to apse longitude ω, because ω appears combined with the true anomaly f. The situation is more complicated for semimajor axis, for this reason and others, as discussed below.

2.2 Semimajor axis toy model

In the equation for da/dt, one must compare T with the much smaller acceleration eR. The crude derivation below compares the net T and R accelerations across an encounter where the perturber is on a circular orbit and the particle is eccentric, emphasizing the role of the particle's eccentricity e and true anomaly f, which appear in equations (1) and (2).

Consider the cartoon in **figure 3**, at a conjunction between the perturbing moonlet M_s (on a circular orbit) and the particle p (on an eccentric orbit), in the frame moving with the moonlet. The heavy dashed lines indicate circular orbit trajectories. The particle's orbit, being eccentric, makes an angle x with the tangential direction, in the rotating frame of M_s. The bold arrow indicates its trajectory over the encounter, with duration P_o/π and projected length $\sim 3s$ along the circular orbit direction, where $s \sim \Delta a$ is the radial separation at conjunction. We calculate the typical inbound and outbound tangential forces T_1 and T_2 at representative average positions r_1 and r_2, respectively, and difference them. To first order in all quantities, $r_1 \sim s + \delta$, and $r_2 \sim s - \delta$, where $\tan x \sim 4ae/3\pi s$ and thus $\delta \sim (3s/4)\tan x \sim ea/\pi$ in the geometry shown (near $f = \pi/2$ which maximizes the asymmetry). In general we expect that δ will scale as $\sin f$ and will include this factor below. Then, approximating with two factors of $\cos(\pi/4)$ projection first from (s $\pm\delta$) onto r_1 and r_2, and subsequently from directions r_1 and r_2 onto the tangential direction, the net tangential acceleration is

$$T = \cos(\pi/4)\left(\frac{GM_s}{r_1^2} - \frac{GM_s}{r_2^2}\right)\sin f = GM_s\cos(\pi/4)\left(\frac{\cos^2(\pi/4)}{(s+\delta)^2)} - \frac{\cos^2(\pi/4)}{(s-\delta)^2)}\right)\sin f, \quad (9)$$

which reduces in the limit $\delta/s \ll 1$ to

$$T = \frac{GM_s}{2s^2\sqrt{2}}\left(-\frac{4\delta}{s}\right)\sin f = -\sqrt{2}\frac{GM_s}{s^2}\frac{ea}{\pi s}\sin f \sim -\frac{GM_s}{s^2}\frac{a}{2s}e\sin f, \quad (10)$$

and we neglect the sign dependence on inner/outer perturber. This is a general result for arbitrary e, a, s, and f in our regime of interest, showing that $T \sim eR(a/2s) \gg eR$ unless $\sin f \ll a/2s$. Thus the T term can dominate the equation for da/dt even when $R \gg T$; in general $ea/2s \sim 0.2$ in the

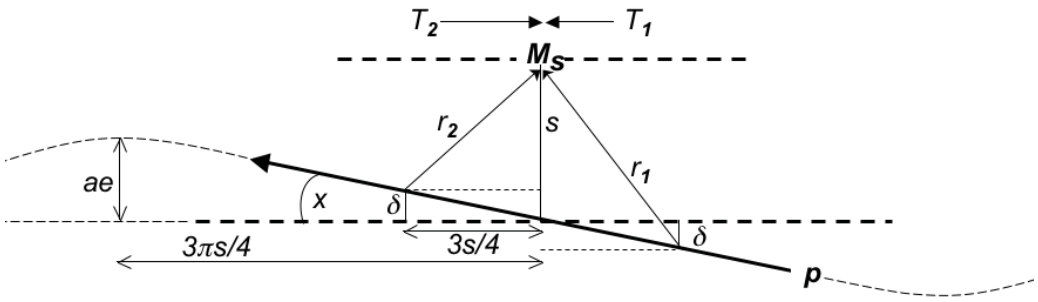

Figure 3: Cartoon illustrating our toy model for semimajor axis perturbations (section 2.2). The perturbing satellite M_s is assumed to be on a circular orbit and the test particle to be eccentric, causing it to encounter the satellite (here at true anomaly of $\pi/2$, which maximizes the asymmetry) with time- and longitude-dependent separation (bold arrow trajectory in frame rotating with M_s). The semimajor axes are separated by s. The angles in question are approximated using the particle eccentric excursion ae and the longitudinal wavelength of the perturbation $3\pi s$. Inbound and outbound tangential perturbations T_1 and T_2 are calculated at average inbound and outbound distances r_1 and r_2.

region of interest, so $R \gg T$ is not grossly violated, but neither is it robustly satisfied. The equation for da/dt then takes a form superficially similar to the toy model equations for $(dh/dt, dk/dt)$:

$$\frac{da}{dt} = (2/n)[Re\sin f + T(1 + e\cos f)] \approx 2T/n \approx \frac{2}{n}\frac{GM_s}{s^2}\frac{a}{2s}e\sin f, \tag{11}$$

so the semimajor axis perturbation over the entire encounter, with duration P_o/π, is $\Delta a = \Delta A \sin f$, where $\Delta A = (P_o/\pi)^2(GM_s/s^2)(ae/2s)$. Putting in the numbers gives us values of Δa between 1-20km for s values typical of the Prometheus-F Ring geometry, consistent with numerical integrations by SB82 and Beurle et al. (2010). The important difference is that the angular argument involves the true anomaly f rather than the mean longitude $g = f + \omega$, and we must consider the change in apse longitudes of the particle and perturber, as well as in their orbit longitudes, from one encounter to the next.

To study the crucial role of periapse motion, we will use a handy trick developed by Showalter and Burns (1982; SB82) to simplify the problem. SB82 studied the dependence of da/dt on the asymmetry of the forces across an encounter in the regime where s is not much greater than ae, using numerical integrations. They showed that the general problem of an encounter between two eccentric objects could be reduced to the simpler problem of an eccentric perturber and a *circular* ring by attributing all the eccentricity to an "effective" perturber, still orbiting at mean motion n_s, and encountered at some "relative longitude" angle Ψ from its pericenter (which is essentially the mean anomaly in their definition but we will conflate in our figures with the true anomaly f for simplicity). The orbit elements of the effective perturber are a combination of those of the actual perturber and the ring particle. Their figure 1b indicates how, over the duration of the encounter (which lasts a fraction of an orbit period), the perturber executes a partial epicycle. SB82 further presented their results as Δa^* in the even more simplified case that the *periapse* longitude of the merged system (which they call ϕ) is zero. They note that their results can be converted to an arbitrary encounter, in which the effective system has relative orbit longitude Ψ and periapse longitude $\phi \neq 0$, using $\Delta a(\Psi, \phi) = \Delta a^*(\Psi - \phi)$. A similar procedure was mentioned by Petit and Henon (1987), based on Henon and Petit (1986). We will simply use SB82's trick of merging the orbits; however, it is cleaner

for our development to assign the relative eccentricity all to the particle and take the perturber orbit as circular.

Figure 4 (upper panel) illustrates the encounter geometry in a frame moving at n_s. The radius of the epicycle corresponds to the degree of apse alignment - larger epicycles (and closer encounters) arise when apses are antialigned. The lower panel, adapted from Beurle et al. (2010), shows the perturbation for an actual encounter as a function of the relative longitude Ψ of the particle ($\Psi \approx f = 0$ if the encounter is at the particle's periapse). The solid and dotted curves in the top and bottom panels are for corresponding mutual apse orientations. Thus in figure 4, the perturbation gets very small when $\Psi \approx f = 0$ as well as vanishing when the relative eccentricity is zero (the dotted curve in the upper panel shrinks to a small radius). In the limit of weak perturbations we see the roughly $\sin f$ dependence in figure 4. The lower panel, adapted from Beurle et al. (2010), shows their numerical calculations of the effect for several different mutual apse longitudes (180° representing antialignment). When the apses are antialigned, $s \ll \Delta a$ so the perturbation has a larger amplitude and deviates from a sinusoidal shape (note however that the curve at 0° is not quite flat).

Motivated by our toy eccentricity model, we will see whether, in the effective semimajor axis perturbation system of SB82 figure 4, successive encounters can occur at angles Ψ which differ by π, such that the successive perturbations Δa cancel, resulting in a stable orbit. Of course, this can happen *exactly* only in the weak perturbation limit when the perturbation has the form of a sine wave.

As noted previously, we choose to merge the eccentricity and apse properties of the perturber-particle system in the ring particle (see figures 4 and 6). That is, we explore the angle

$$\Psi_{i+1} - \Psi_i \approx f_{i+1} - f_i = (g_{i+1} - \omega^*_{i+1}) - (g_i - \omega^*_i) = g_{i+1} - g_i - (\omega^*_{i+1} - \omega^*_i) = n_o P_{syn} - (\omega^*_{i+1} - \omega^*_i). \tag{12}$$

The explicit change in periapse longitude $\omega^*_{i+1} - \omega^*_i$ of the combined system (the ring particle) is the key difference between the da/dt system and the de/dt system. We now recall that, in the notation of SB82, the periapse longitude ω^* of the merged, "effective" system is their angle ϕ (see SB82 figure 2), which is given by

$$\tan\phi = \frac{a_s h_s - a_0 h_0}{a_s k_s - a_0 k_0} \sim \frac{h_s - h_0(1 + s/a)}{k_s - k_0(1 + s/a)} \sim \frac{h_s - h_0}{k_s - k_0} \sim \frac{\sin\omega_s - \sin\omega_0}{\cos\omega_s - \cos\omega_0}. \tag{13}$$

where we have used the facts that $a_0 = a_s + s$, $s \ll a_0$, and assumed $e_s \sim e_0$. A few trig identities lead us to

$$\tan\phi = -\frac{\cos((\omega_s + \omega_0)/2)}{\sin((\omega_s + \omega_0)/2)} = -\cot((\omega_s + \omega_0)/2); \tag{14}$$

and thus $\phi = (\omega_s + \omega_0 + \pi)/2$. Setting $\omega^* = \phi$ and resuming from equation (12) above,

$$\Psi_{i+1} - \Psi_i = n_o P_{syn} - (\phi_{i+1} - \phi_i) = n_o P_{syn} - [(\omega_s^{i+1} - \omega_s^i) + (\omega_0^{i+1} - \omega_0^i)]/2. \tag{15}$$

The precession rates of Prometheus and the F Ring differ by less than 2%, so even though they both precess by a significant angle over the synodic period between encounters i and $i+1$, these precession angles differ by only a few percent and are moreover averaged in equation (15) above, so we will set the apse precession rates and angles equal for the purpose of the toy model.

$$\Psi_{i+1} - \Psi_i \approx n_o P_{syn} - (\omega^{i+1} - \omega^i) \approx n_o P_{syn} - \dot{\omega} P_{syn}. \tag{16}$$

We now recall that for a particle at some fractional distance $0 < \epsilon < 1$ from some Lindblad resonance of order m, the synodic period is $P_{syn} \approx (m + \epsilon) P_o$ where $P_o = 2\pi/n_o$ is the particle's orbit period. Then keeping the most significant terms,

$$\Psi_{i+1} - \Psi_i \approx n_o(m+\epsilon)P_o - \dot{\omega}(m+\epsilon)P_o \approx (m+\epsilon)n_o P_o - (m+\epsilon)\dot{\omega}\frac{2\pi}{n_o} \approx 2\pi m + 2\pi\epsilon - \frac{2\pi m\dot{\omega}}{n_o}. \tag{17}$$

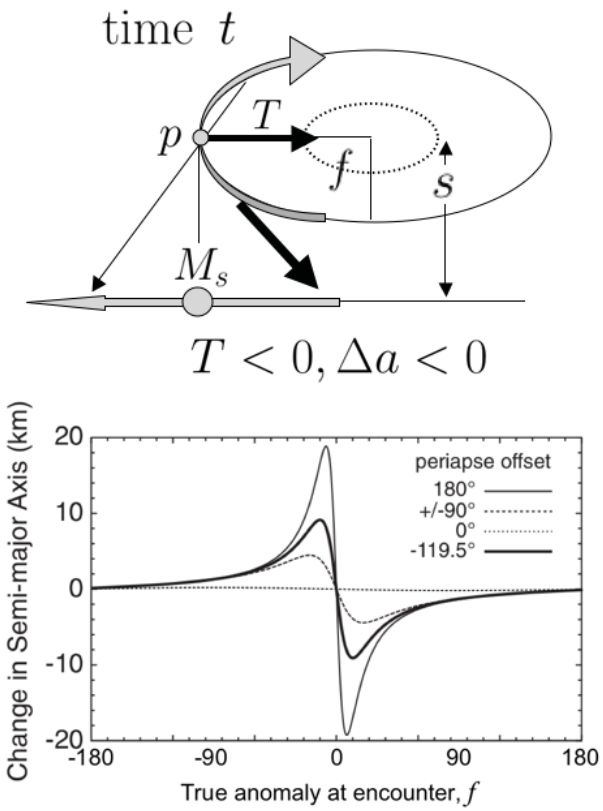

Figure 4: Depiction of encounter geometry following SB82, in which all the eccentricity is assigned to the (outer) object, which in our case we choose to be the ring particle p, leaving the perturbing satellite M_s on a circular orbit. Upper panel: an encounter at particle true anomaly $f = \pi/2$ leads to a negative tangential force T and negative semimajor axis perturbation Δa. This is because the negative acceleration experienced by p when it is closer to the incoming satellite is larger than the positive acceleration it experiences from the outgoing satellite, when the objects are further apart. Lower panel (adapted from Beurle et al. 2010): semimajor axis perturbation as a function of f for two orbital configurations corresponding to apse antialignment (light solid) and orthogonal (dashed). In the closer, stronger encounters, the peak perturbation is not experienced at $f \sim \pm\pi/2$, but the $\sin f$ limit of our toy model is approached in the weak perturbation limit.

The first term in the final expression, $2\pi m$, can be ignored as it simply represents an integer number of full rotations of $\Psi_{i+1} - \Psi_i$. Thus we end up with

$$\Psi_{i+1} - \Psi_i = 2\pi \left(\epsilon - \frac{m\dot{\omega}}{n_o} \right). \tag{18}$$

Recall that, similarly to the toy eccentricity model, successive perturbations cancel when $\Psi_{i+1} - \Psi_i = \pi$, so the condition for stable semimajor axis is

$$\left(\epsilon - \frac{m\dot{\omega}}{n_o} \right) = \frac{1}{2}. \tag{19}$$

In fact, throughout the F Ring - Prometheus region, apses do precess by nearly a half cycle in one synodic period, with only slow variation over hundreds of km (see **figure 5**). In fact, near the

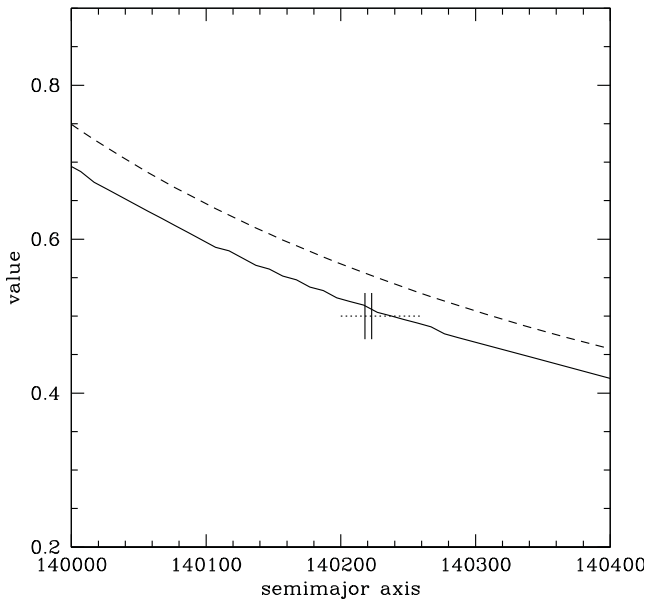

Figure 5: Slow variation over the F Ring region of two quantities: the dashed curve shows the ratio P_{syn}/P_o (divided by 200) and the solid curve shows the ratio $(m\dot{\omega}/n_o)$. Note how the latter ratio is extremely close to 0.5 at the F Ring's actual location, bounded by the vertical lines. It is not a requirement of the model that the ratio be *exactly* 0.5, but proximity to this value brings the stable zones closer to LRs.

nominal location of the F Ring core at 140220km, a Lindblad Resonance (LR) lies where the parameter $m\dot{\omega}/n_o = 0.5008$! Throughout this regime, the "prompt" successive-encounter cancellation of semimajor axis perturbations is satisfied *at* nominal Lindblad resonance locations, where $\epsilon = 0$ (equivalently $\epsilon = 1$). This is a somewhat counter-intuitive result, and we emphasize that it is not a general property of Lindblad resonances, but a wrinkle occurring under certain *additional* conditions involving both the apse precession rate *and* the proximity of the particle to its perturber (through m). The condition is not satisfied in normal, low-order LRs, where m is not large, since $\dot{\omega}/n_o \ll 1$. Indeed, using our numerical models, we verified that each low-order LR is characterized by relatively *large* RMS fluctuations in both a and e. In the limit $\dot{\omega} \to 0$ the simpler AR criterion ($\epsilon = 1/2$) is recovered. We have not searched for other planetary ring or exoplanet applications which might be found for this unusual combination of properties. Cooper et al. (2012) have noted empirically that an equivalent relationship characterizes the F Ring core, expressing it as $n_s - n_F \approx 2\dot{\omega}$; it is simple to show that this is the same relationship required in equation 19 for stable zones to lie at Lindblad resonances ($m\dot{\omega}/n_o = 0.5$). Cooper et al. (2012) also note that this relationship would lead to the sort of cancellation that we describe in more detail here.

The essence of the physics is illustrated in **figure 6**. The ring particle p executes epicycles with frequency $\kappa_o = n_o + \dot{\omega}$ about its guiding center, which moves with mean motion n_o. A test particle returns to reencounter M_s after a synodic period $P_{syn} = 2\pi/|n_o - n_s|$. Note that the lower panel shows a case where $P_{syn} = 2\pi/|n_o - n_s| = 2\pi m/\kappa_o$, which is easily rewritten as $\kappa_o = m|n_o - n_s|$, the condition for a Lindblad resonance of order m (see Appendix A). Yet, because of the ensuing precession of the (merged) apse by π during P_{syn}, the situation behaves like an antiresonance (top panel) would in the more normal situation where differential precession is unimportant. Note that in

the strong perturbation limit (lower panel of figure 4), the peak positive and negative impulses are not separated by π in f; here the analysis is more complicated than can be addressed in a toy model because the period of p changes as a result of the encounter, changing its epicycle frequency κ and the synodic period.

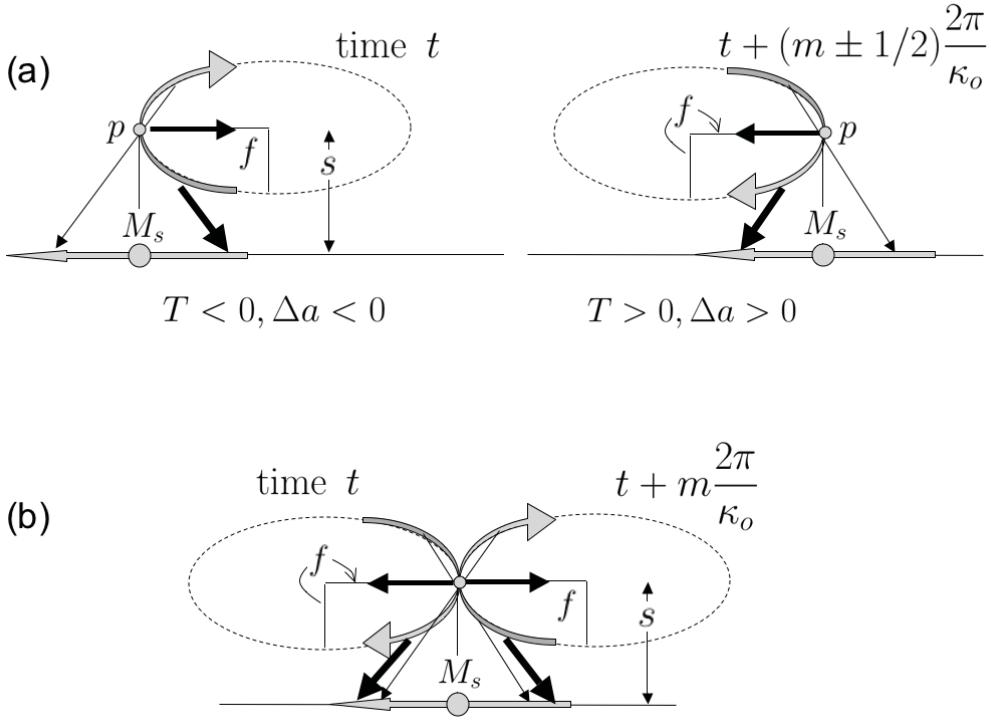

Figure 6: Illustration of two ways of producing prompt cancellation of a previous perturbation, following the geometry of figure 4. Upper panel: when there is no periapse precession, the negative perturbation Δa at time t can only be promptly canceled if the subsequent encounter occurs at a time when p is off by one-half cycle from an integer number of epicycles. An integer number of epicycles for p between encounters would represent a Lindblad resonance of order m, so we call the situation of the upper panel an antiresonance; a particle would be in such a state if its semimajor axis lay halfway between resonance locations. The lower panel shows how a resonant semimajor axis *per se* can lead to prompt cancellation if, during the synodic period between encounters, the apse longitude of p (in the merged system) has precessed by exactly π so p is now moving outwards instead of inwards at encounter. This case, where $P_{syn} = 2\pi m/\kappa_o$, occurs at a Lindblad resonance (see Appendix B).

3 Results from numerical integrations

In this section we present numerical integrations, using our Bulirsch-Stoer integrator (see Appendix B for details). In general we initialize 14 massive perturbing satellites (Atlas through Iapetus and even Phoebe) using a state vector from Bob Jacobson (personal communication 1994, 2010, 2012) containing positions and velocities at epoch January 2, 2004. We initialize our thousands of test particles over some range in a, with some initial e, and randomly distributed orbit and apse longitudes and zero inclination (the inclination slowly grows). The integration proceeds in cartesian position-

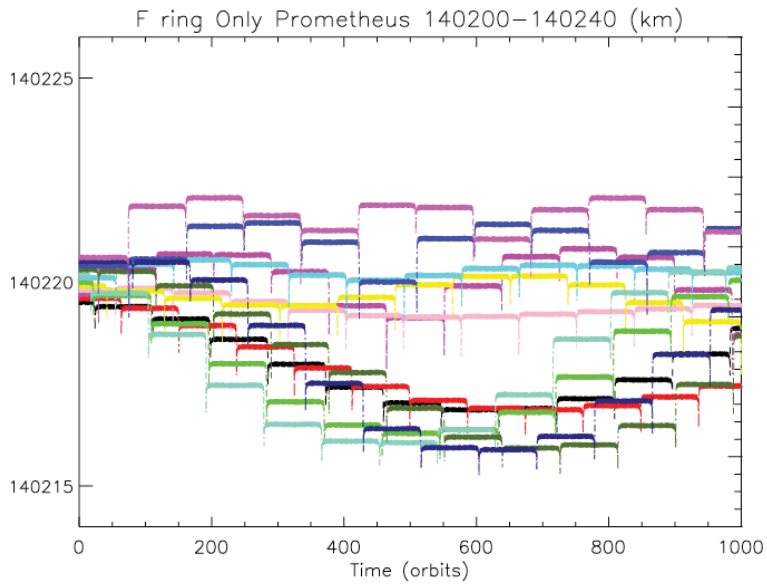

Figure 7: A short time evolution (1000 Prometheus orbits) with Prometheus as the only perturber. Note the cyclic, step-like evolution of the semimajor axis for the set of initially closely spaced particles shown. Each step occurs at Prometheus encounter. Different cyclic periods and amplitudes correspond to different distances from resonance. Compare with figure 2b. A greyscale version of this figure will be provided for the print version.

velocity space, and we convert these properties to epicyclic orbital elements following the approach of Borderies-Rappaport and Longaretti (1994).

3.1 Short time histories for test particles

Here we show short runs with a small number of particles to illustrate the general properties of the ensemble. **Figure 7** shows a very short run, here with only Prometheus as perturber, showing the evolution of semimajor axes of 11 test particles with closely spaced initial values. The semimajor axes change impulsively and only at encounters with Prometheus (as in figure 2b). The cyclic stairstep pattern is close to that predicted by the toy model for a case when the apses are not close to antialignment and the impulses are weak (here the strongest impulses are about 1km). Notice how the amplitude of the semimajor axis cycle varies with location. This is because the test particles, not in general being in resonance with Prometheus, re-encounter it each time at a slightly larger value of Ψ, so the perturbation slowly cycles from positive values to negative ones. Because the changes here are small, the test particle period is not changed significantly and the cycle has a regular appearance.

Figure 8 shows a longer run, now with all 14 perturbing satellites active, showing the evolution of semimajor axes of test particles with closely spaced initial values. The semimajor axes change impulsively and primarily at encounters with Prometheus (still spaced by $P_{syn} \sim 100 P_o$ as above, and still visible). A larger variety of patterns is seen because of the complicating effects of Pandora and the other moons. Still, cyclic patterns are seen at some locations, while some other locations show very little change in semimajor axis even over this long duration run (10000 Prometheus orbits or about 16.8 years).

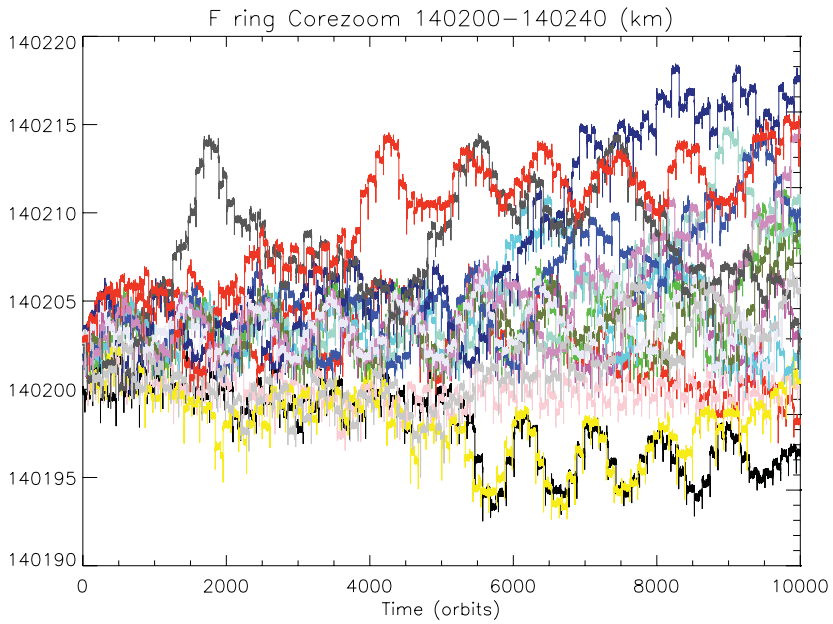

Figure 8: A different evolution, over a longer time (10000 Prometheus orbits), and including the effects of all perturbers. Individual impulses spaced by roughly 100 Prometheus orbits can be seen. A greyscale version of this figure will be provided for the print version.

3.2 Validation of toy model physics

To help us build confidence in the somewhat counterintuitive predictions of the toy model, we used our code NBODY to run a series of cases in which the planetary oblateness was systematically varied over a small range (see Appendix B for a description of the code numerics). The purpose of this is to test the robustness of the prediction that stable zones track LRs, over a wide range of apse precession periods. To simplify the case and get a situation as close as possible to that of the toy model, we removed all the inner ringmoons except Prometheus; we do not expect the absence of these other small moons to have any zero-order effect on the integrations over this short period (our full integrations contain all the ringmoons). By virtue of our initial conditions, which used cartesian positions and velocities of the gravitationally active moons (R. Jacobson, personal communication, 1993, 2008, 2012), a change in planetary oblateness leads to a change in the consistently determined semimajor axis of "Prometheus", so we have a suite of cases in which the perturber takes on a range of semimajor axes, while the planetary oblateness factors J_2, J_4, J_6 are scaled by a factor $F_J = 0.6$ to 1.5 times their nominal values (see table). Thus the typical resonance order m and radial spacing in the region of interest changes. Since the locations of the LRs move around considerably, the results allow us to track how faithfully the toy model predictions are obeyed, in the real case, over a range of conditions.

We demonstrate this by calculating the statistical RMS deviation of the time-dependent semimajor axis $a(t)$, as a function of its average value, for all test particles, initialized on a fine grid with radial spacing of about 10 m, and run (in this case) for 5000 Prometheus orbits (about 8.4 years). That

is, for each test particle, we calculate an average of, and RMS deviation from, the semimajor axis for the duration of the run. Only particles which never deviate far from their initial values can have an extremely low RMS in this sense. As shown in section 3.3, particles initialized elsewhere can become *trapped* into stable orbits but, as their starting radius is different, the average will be different and the RMS larger than the most stable semimajor axes. We will make use of plots like these subsequently for the full-up runs, but here we use them to assess the nature of the most stable orbits and test the toy model.

The results are shown in **figure 9** (F_J=0.6-1.0). Notice the narrow clusters of points - no more than a km wide - having very low RMS deviation (less than 1 km). The red triangles represent Lindblad resonance locations for the satellite and oblateness parameters of each run. The small deviations of the stable zones from *exact* LR positions could be due to a number of approximations, to the uncertainty in assumed perturber semimajor axis, or to the fact that $m\dot{\omega}/n_o$ is rarely *exactly* 0.5. Similar results were found for F_J=1.0-1.5. The results support the idea that stable locations appear very close to LRs, in this special regime.

Weak secondary clusters showing low semimajor axis RMS appear halfway between first-order resonances; these are, however, short-lived (the runs shown in figure 9 only covered 5000 Prometheus orbits). We believe these are caused by the same prompt-cancellation physics involving apse precession, and are associated with the weaker second-order resonances that lie halfway between first-order resonances.

3.3 Evolutions for several different regions

With all 14 massive perturbing objects (Atlas through Iapetus, and Phoebe) accounted for, we calculate time histories for three different regions for 10000-20000 Prometheus orbits. The complete cycle of differential apse rotation between Prometheus and the F Ring takes about 16.9 years - also about 10000 Prometheus orbits (Chavez 2009, French et al. 2012). We define the F Ring core region between 140160-140280 km. We also define an "intermediate" region lying between 140350-140470 km (nearly intermediate between Prometheus and Pandora); reference to figure 1 shows that, in this region, Pandora resonances become more numerous and more comparable to Prometheus resonances in strength than in the region where the F Ring core itself lies. We also study a narrower region closer to Prometheus, from 140000-140080 km, located in the vicinity of a new "strand" observed to form over a range of semimajor axis in 2008, apparently created by an unusually vigorous collision between 2004S6 and the F Ring core (Murray et al. 2011). In each case we blanket the region with enough test particles such that their average radial "resolution" is only 10 meters. For instance, the F Ring core region was run in three swaths of 40 km width, each containing 4000 particles. The orbit, node, and apse longitudes are randomly distributed. Thus there is no special moment of "apse antialignment" for the F Ring as a whole, but each particle feels the effects of antialignment at a different time.

The initial eccentricities are taken to be 2.5×10^{-3}. We have found that characteristic eccentricities of this magnitude arise from near-zero initial values after roughly 10^6 Prometheus orbits, a few thousand years (see **figure 10**). It is thus not implausible that typical F ring eccentricities with magnitudes of roughly 2.5×10^{-3} (for the core, strands, and associated objects such as 2004S6) might grow slowly from very small values to their current values over a timespan of a few million Prometheus orbits. However, there might be other explanations. However, note in particular that there is no tendency in our model or numerical integrations for our test particles to *align* their eccentric orbits to a common apse, as observed for the F Ring. See Discussion for more on this.

Time evolutions for nine test particles in each of these three regions, selected almost randomly to represent the gamut of observed behavior, are shown in **figures 11 - 13**. The particles selected

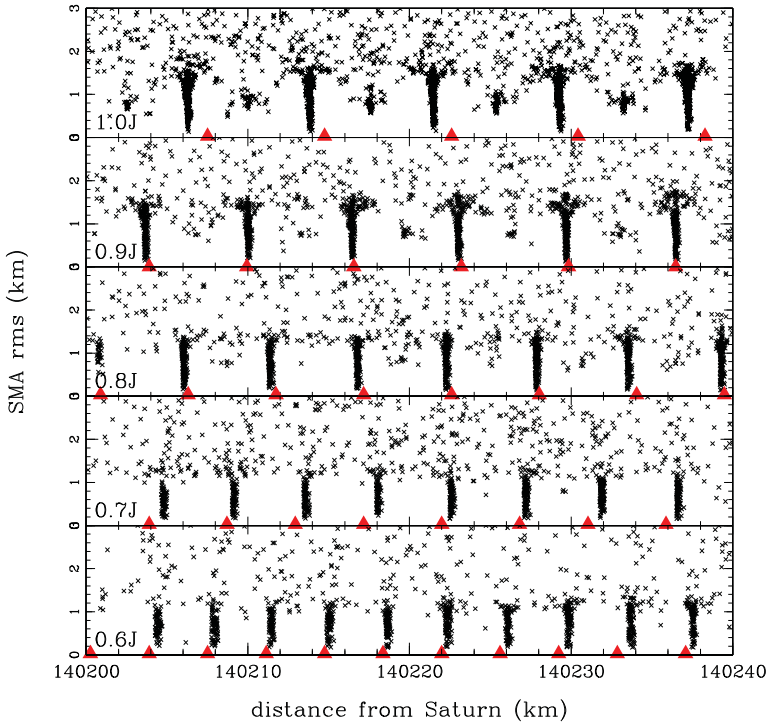

Figure 9: For each particle we plot the RMS deviation in semimajor axis a as a function of mean semimajor axis, over 5000 Prometheus orbits. Narrow vertical clusters lie at mean a where extremely low RMS deviations occur. Red triangles denote first order Lindblad resonances with the single perturbing satellite, nominally "Prometheus" but whose semimajor axis changes as the oblateness parameters J_2, J_4, J_6 are scaled - here by 0.6 to 1.0 of their nominal values. This variation in the location of the perturber causes the separation between resonances to change. The plot shows how stable zones lie very close to first-order Lindblad resonances over a wide range of parameter space. See discussion in section 3.2.

in each case are initially separated by only 10m, covering 80m total, but the starting location was selected to illustrate a representative set. Note that the figures have different vertical scales. Particles quickly separate by several km and then essentially diffuse in semimajor axis, at different rates.

Figures 14 - 16 extend the analysis technique of section 3.2 to these three regions and several different evolution times. The mean semimajor axis $\overline{a}$ and RMS deviation about $\overline{a}$ are calculated for each particle, over the duration of the run. The typical RMS values decrease away from Prometheus, from roughly 20 (as large as 80) km in the 2008 strand region (figure 13), through 10 (as large as 30) km in the F core region (figure 12), to roughly 8 (as large as perhaps 20) km in the "intermediate" region (figure 11). Particles with a combination of semimajor axis and eccentricity allowing them to cross the orbit of Prometheus are colored cyan; clearly this is common in the 2008 strand region and rare elsewhere.

At the same time, we see narrow zones of high stability in all regions. These stable regions align more or less with first-order Lindblad outer resonances of Prometheus (open triangles). It is notable that, in the intermediate region, the most stable zones are somewhat shallow, with few particles retaining RMS values less than 1.5-2 km. On the other hand, the stable zones seen in the F Ring core radial region and even in the 2008 strand region, are deeper, with RMS deviations routinely extending

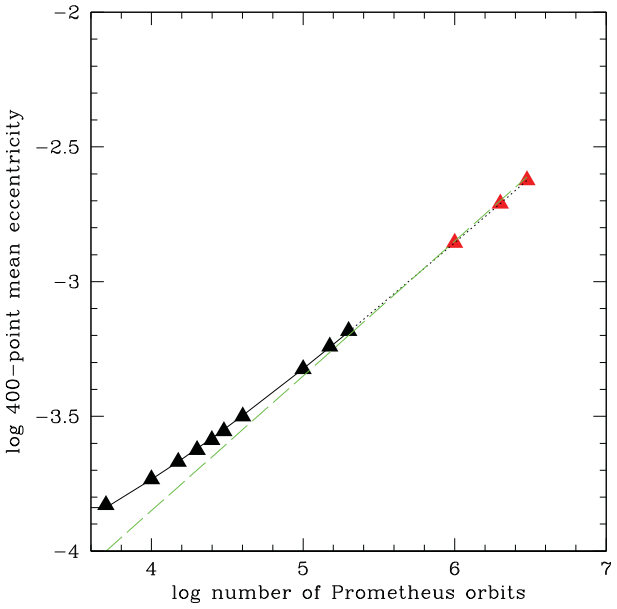

Figure 10: We ran (in stages) a very long case in the F Ring core region (to 200000 Prometheus orbits), with all test particle eccentricities initially set at zero, to assess the growth of ensemble eccentricity (series of black triangles). We fit a curve to the results (black smooth curve) and used it to extrapolate forwards to longer times (red triangles). After the very early stages, the mean eccentricity grows as $t^{1/2}$ (green dashed line).

to the km-or-less level (**Figures 15** and **16**).

We note that in all regions, the proximity of occasional Pandora resonances to Prometheus resonances reduces the depth of the stable zones. The stable zone closest to the nominal semimajor axis of the F Ring core strand (140223km; Bosh et al. 2002) is somewhat complicated and disturbed by a Pandora resonance, and in the 2008 strand region, potentially stable zones at two Prometheus resonances in the region studied are entirely destabilized by nearby Pandora resonances over the time of our evolutions (15000 Prometheus orbits). Recall that Pandora resonances move around because the semimajor axis of Pandora oscillates by several km over a period of a few years under the influence of Mimas (see figure 22). While the ensuing effects are properly captured in the NBODY runs, the resonance locations shown as symbols in figures 14 - 16 are only the mean values. The effect of this is a subject worthy of future study.

Notice in model runs in French et al. figure 8, which *do not include* perturbations from Prometheus or Pandora, the relatively low-order resonances with Janus/Epimetheus show *enhanced* RMS, as expected for *low-order resonances*, where our model suggests that apse precession cannot lead to prompt cancellation of the prior perturbation because the synodic period is too short.

On the whole, Prometheus first order resonances provide safe havens from the large and changeable semimajor axis perturbations that particles will, in general, experience across the entire region sampled. However, these "antiresonances" seem quantitatively less stable *further* from Prometheus (in the intermediate region) than closer (in the F core region), in the sense of having shallower RMS semimajor axis deviation minima further from Prometheus. This is almost certainly due to the increasing relative strength of Pandora resonances relative to the F core region, where the Prometheus first order resonances, while stronger, are more cleanly separated and isolated from other effects (see

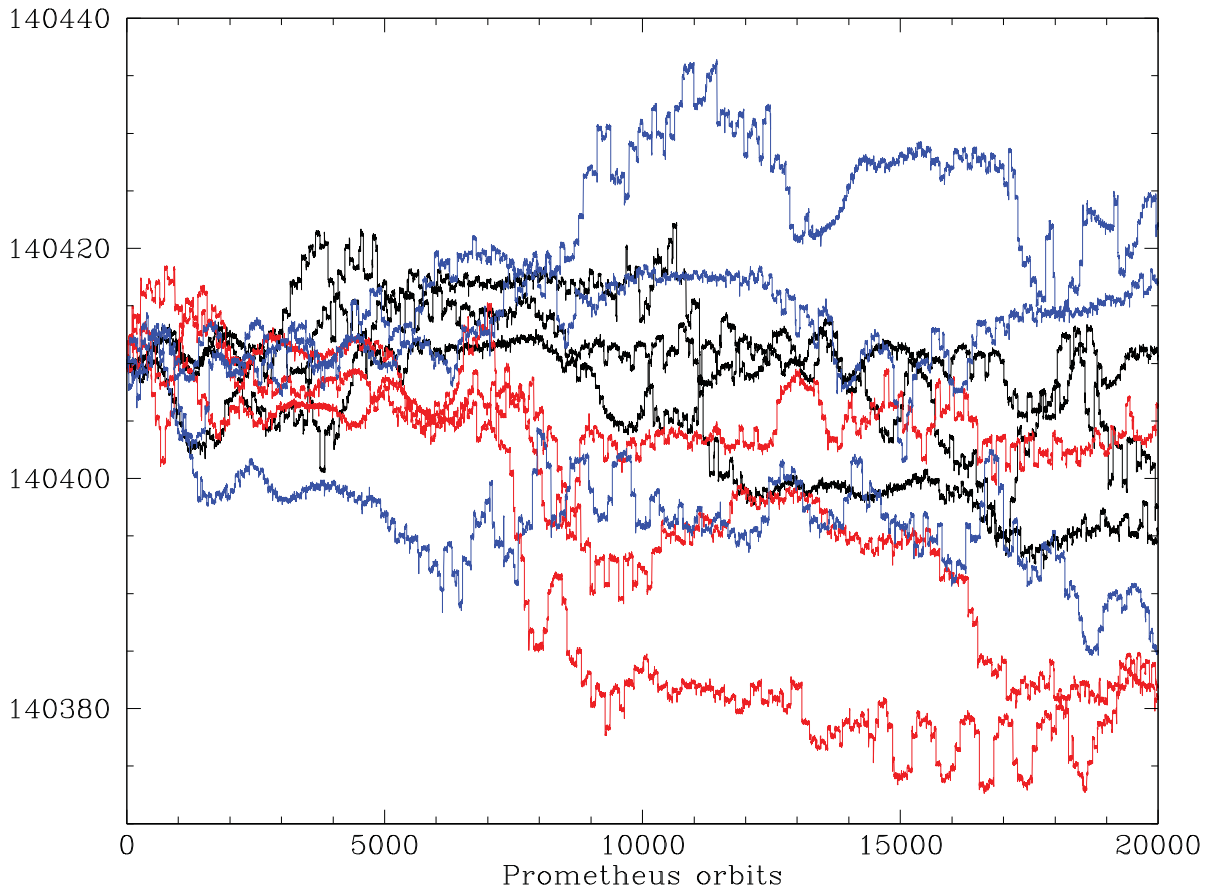

Figure 11: An evolution for the "intermediate" radial range 140350-140470 km (see figure 1). The sample shows nine particles chosen to illustrate representative evolutions, all initially lying with semimajor axes spaced by ten meters. Impulses can be seen at Prometheus encounters, and the particles diffuse over roughly $\pm$ 20 km over the run, showing little tendency for temporary stability. Note that figures 11,12, and 13 have different vertical scales.

figure 1 and French et al. 2003). In the 2008 strand region, perturbations are much stronger and more sensitive to small changes in the encounter true anomaly, changing the semimajor axis and period, and are thus harder or impossible to cancel exactly over long periods of time.

3.4 Diffusive behavior with trapping at stable radii

In this section we describe the *ensemble* behavior of particles in these three zones, given the temporal behavior seen in figures 11-13 and the semimajor RMS deviations seen in figures 14 - 16. As suggested by figures 11-13, particles display a diffusive behavior in semimajor axis a, at least qualitatively. For example, **figure 17** combines all test particles and shows the probability distribution functions (PDFs) of final-initial semimajor axis $(a_f - a_i)$ as a function of location and time. The narrowest distribution is seen in the "intermediate" region, 140350-140470 km, which is farthest from Prometheus. The PDFs broaden closer to Prometheus, with the 2008 strand region having the broadest distribution after 10000 Prometheus orbits (most vigorous diffusion). Notice, however, its PDF is

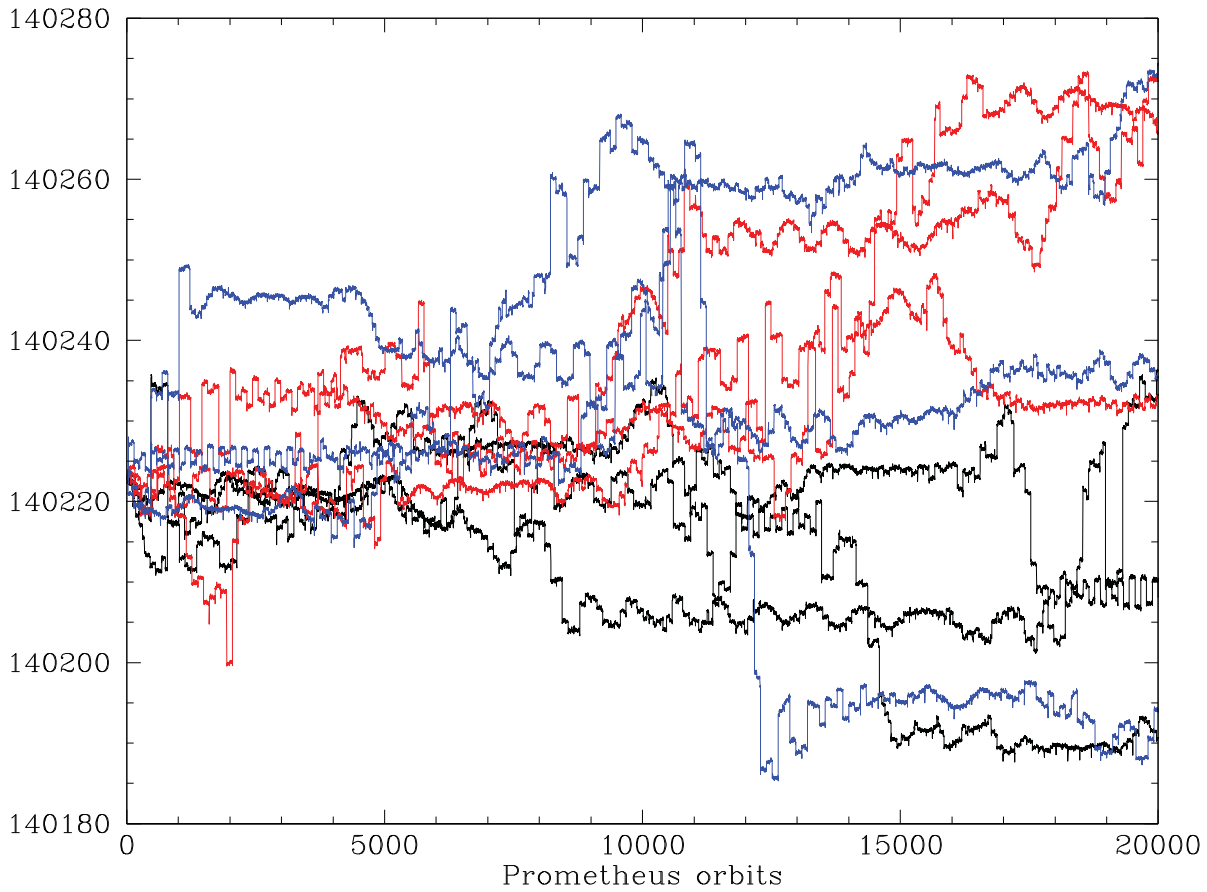

Figure 12: An evolution for the F Ring core radial range 140160-140280km (see figure 1), as in figure 11. The particles diffuse over roughly $\pm$ 40 km over the run, but show some tendency for temporary stability. For example, there are six or seven time periods, in different trajectories, when semi-regular oscillations in a occur with amplitude of 2-3 km, over durations of 5000-10000 Prometheus orbits. Note that figures 11,12, and 13 have different vertical scales.

more centrally spiked than the expected Gaussian for a true diffusion process; we discuss this more below. Particle radial density PDFs for the F core region, at three different times, show the expected broadening as time proceeds.

The situation is demonstrated in yet a different way in **figures 18 - 20**. These figures present binned histograms of particle number per bin of mean semimajor axis, for the three regions, each showing two different evolution times. In each figure, the horizontal line above the histogram indicates the initial distribution of particles, both in radial extent and in number per radial bin. The plots show a clear radial diffusion out of the initial radial range in each case, with the diffusion being the most vigorous in the 2008 strand region and the most sluggish in the "intermediate" region. Also apparent in these figures is an enhanced population of particles at a number of discrete radii. These are the stable, low-RMS radii of figures 14 - 16. The overall properties of figures 18 - 20 follow from the behavior seen in figures 14 - 15. The characteristic semimajor axis RMS decreases away from Prometheus because the amplitude of each individual impulse decreases and thus decreases the particle diffusivity.

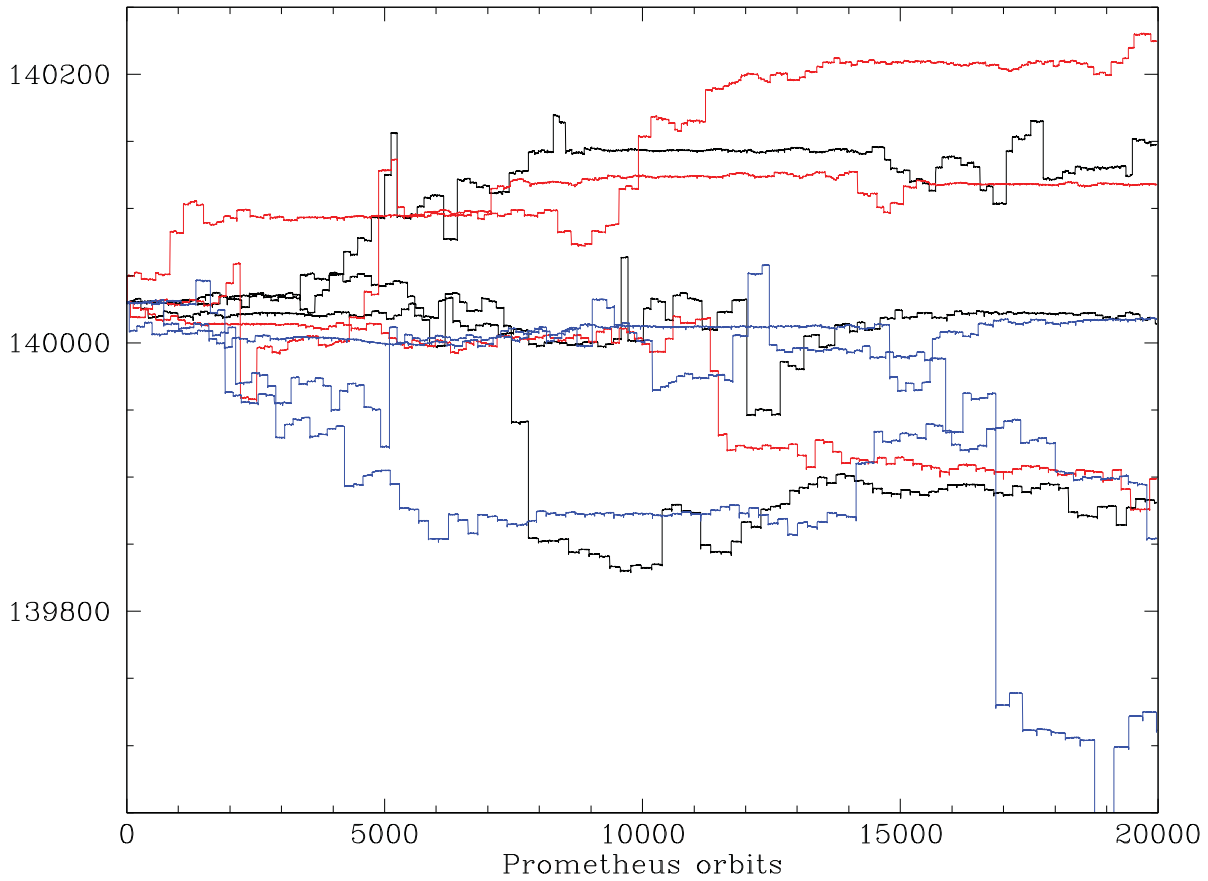

Figure 13: An evolution for the radial range 140000-140080km characterizing the 2008 strand (see figure 1), as in figure 11. Impulses can be seen at Prometheus encounters, some quite strong (>20 km). The particles diffuse over roughly $\pm$ 250 km over the run, and show some tendency for temporary stability. Here, stretches longer than 5000 orbits can be seen in which fluctuations in a hardly register on this vertical scale, but are consistent with those seen in figure 12. Note that figures 11,12, and 13 have different vertical scales.

An effective diffusion coefficient can be constructed from these semimajor axis perturbations if each is regarded as independent. If the perturbation is larger than several km, as it often is, the orbital and synodic periods are changed so the particle re-encounters the satellite perturber at a (merged) true anomaly that is not simply predicted as in our toy model, so the perturbations are quite independent and largely unpredictable. Thus we enter a truly chaotic situation, which can be approximated as radial diffusion in semimajor axis with a diffusion coefficient $\mathcal{D} = \Delta a^2/P_{syn}$. Here Δa would be the "typical" perturbation for particles that do not lie at a stable antiresonance radius. For instance, equation 11, Beurle et al. (2010), and SB82 give impulse amplitudes of $\Delta a \sim$ 1-20 km in the F core region, smaller in the "intermediate" region, and larger in the 2008 strand region, which are in agreement with the numerical simulations. If "typical" values in the F core region are 1-5km, we can estimate the radial diffusion length L of particles using $L^2 = \mathcal{D}t$; in 10000 Prometheus orbits (about 17 years), $L \sim$ 10-50 km, and $L \sim$ 100-500 km in 1700 years. Clearly, bodies within the F Ring core do not share the chaotic properties of typical objects in their very near vicinity.

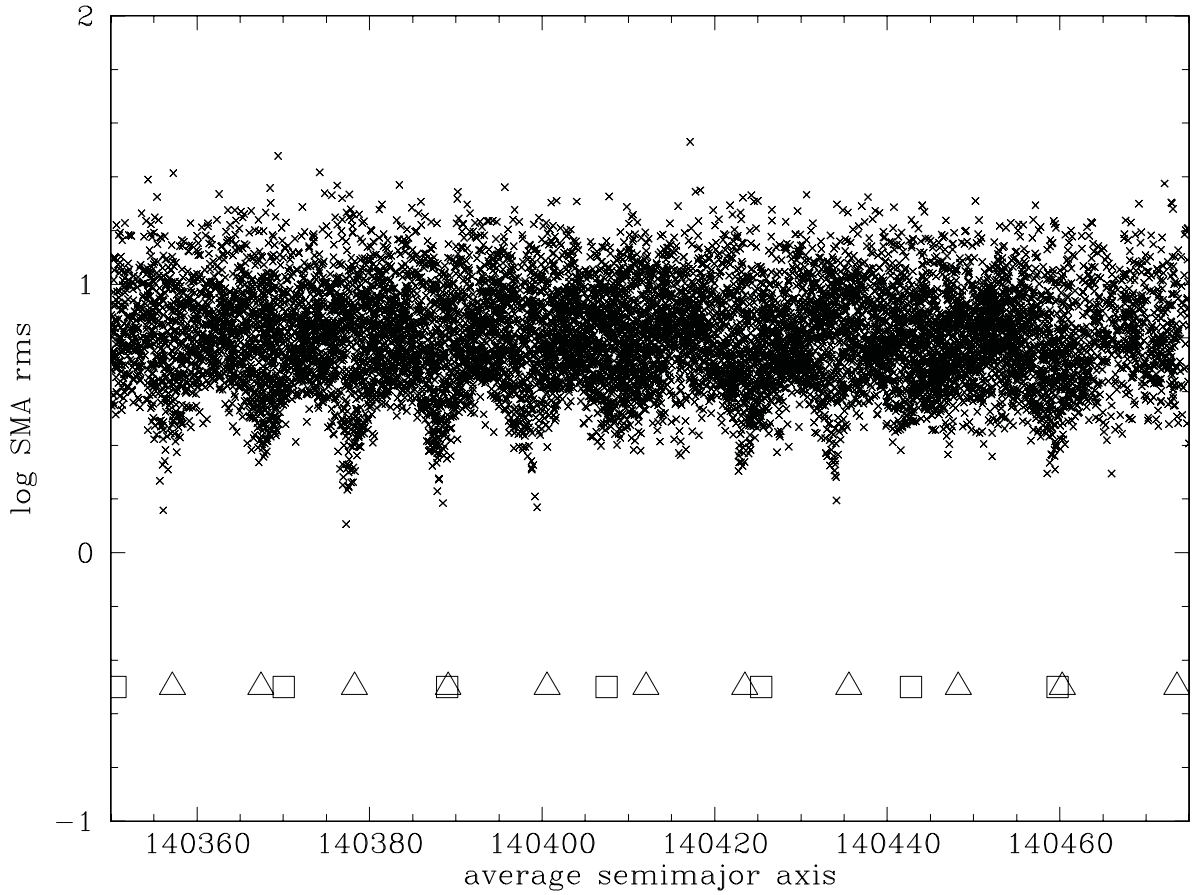

Figure 14: The log of the RMS deviation in a (km), as a function of mean semimajor axis a, for 12000 particles in the "intermediate" radial range 140350-140470 km (see figure 1), taken over a duration of 20000 Prometheus orbits. The plot illustrates the total range of RMS and the fine structure in stable, low-RMS zones. The locations of first-order resonances with Prometheus (triangles) and Pandora (squares) are shown. Note that few particles have semimajor axis RMS less than 2 km, and typical RMS values are less than 15-20 km.

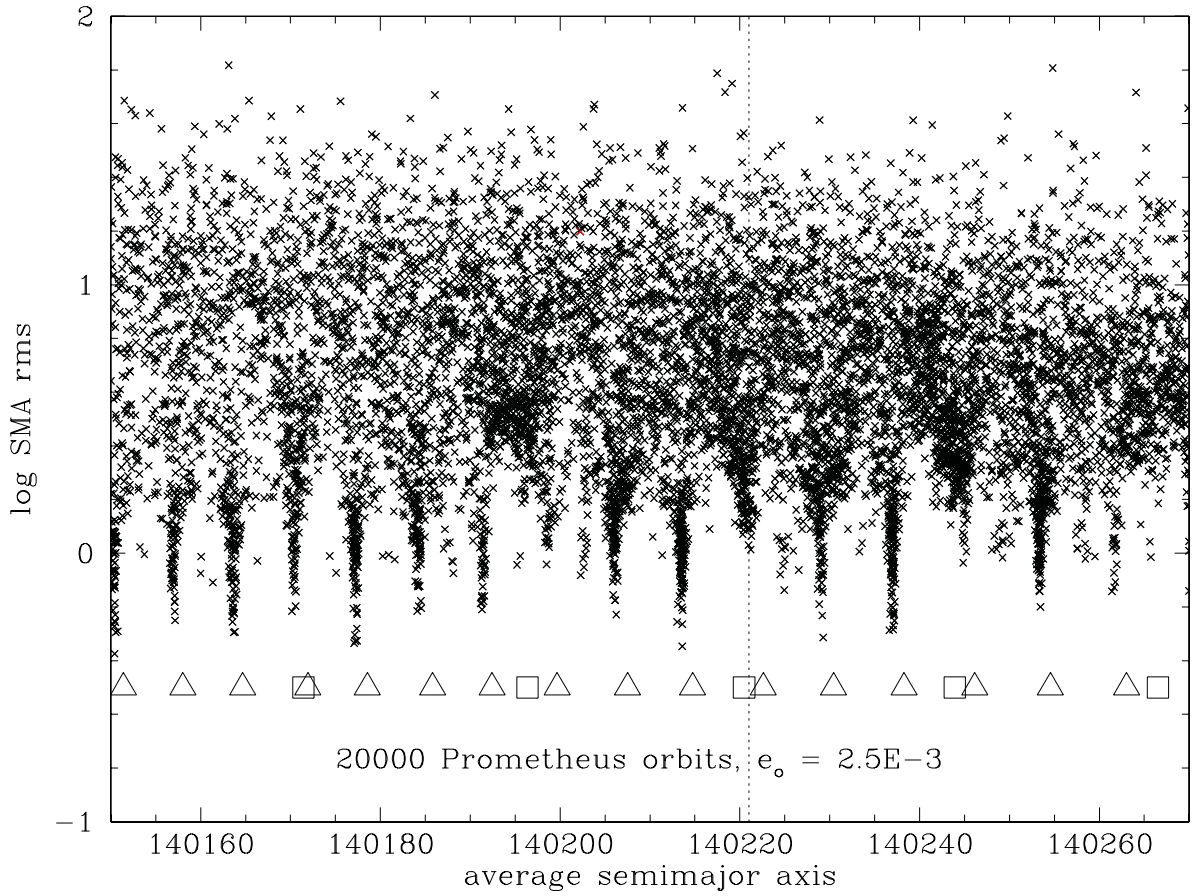

Figure 15: As in figure 14, but for the F Ring core radial range 140160-140280 km. Note that nearly all the stable zones have semimajor axis RMS less than 1km, but typical RMS values are now up to 30km or more. The vertical dotted line is the average of the Albers et al. (2012, "fit 2") and Cooper et al. (2012, "fit 12") solutions for the F Ring semimajor axis: 140221.3±1.8 km and 140220.8±0.3 km respectively. The observed a thus aligns nicely with a prominent predicted stable zone, even though slightly stirred by a Pandora resonance (see section 4). Note for comparison that the standard F Ring semimajor axis of Bosh et al. (2002) is 140223.7±2.0 km

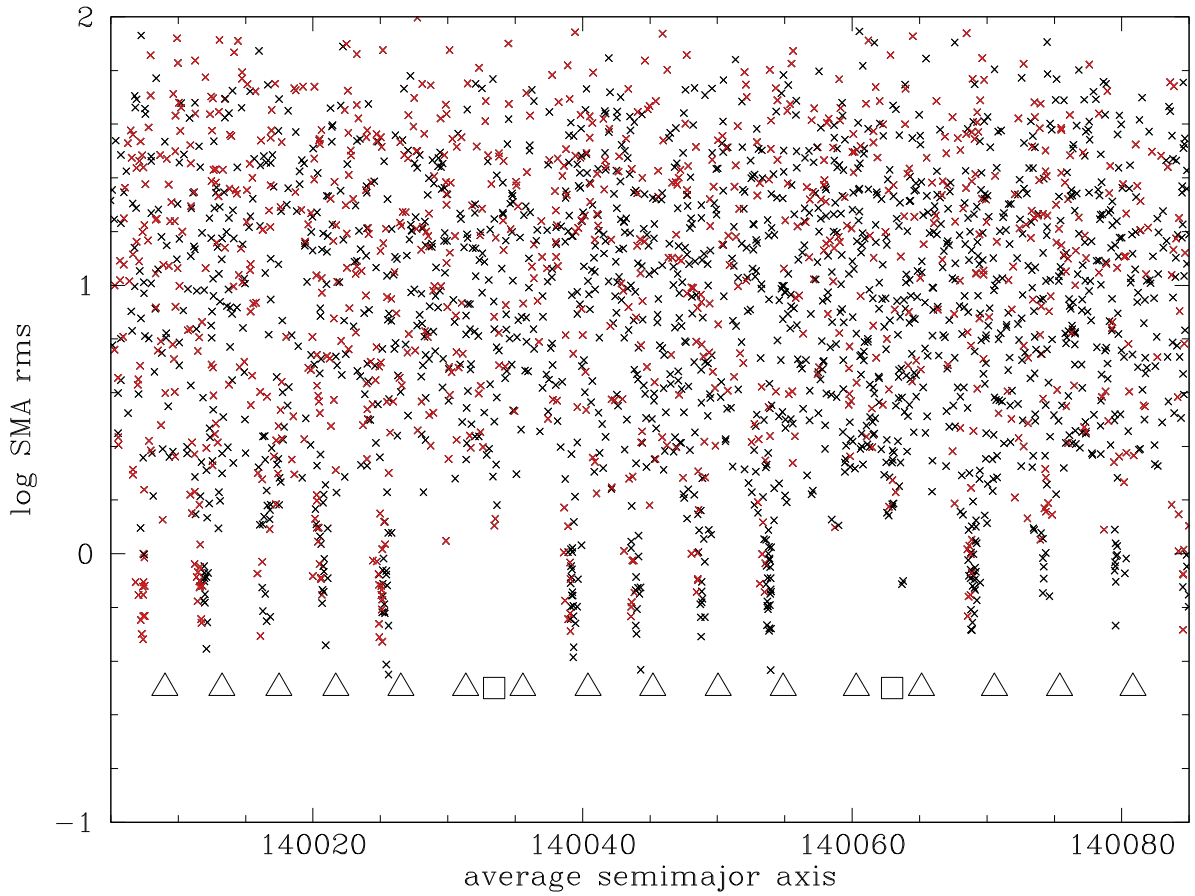

Figure 16: As in figure 14, but for the radial range 140000-140080 km characterizing part of the 2008 strand, and for a duration of 15000 Prometheus orbits. Here and in figure 15 (where only one can be seen) particles crossing the orbit of Prometheus are shown colored red in the online version. Pandora resonances have destabilized several otherwise stable zones, but the remaining ones have semimajor axis RMS less than 1km. However, typical RMS values are now up to 70-80 km, or larger.

Quantitatively, we can see that in the intermediate region, the average particle number density is not changing much through the region initially populated, although some particles are leaking away at the edges (compare horizontal line showing initial population per bin with the histogram). However, in the 2008 strand region, the particle density is steadily and rapidly declining throughout the initial region. The exceedingly rapid diffusion within, and depletion of, the 2008 strand region may be partly due to the fact that many of these particles cross the orbit of Prometheus (cyan points in figure 16). However, as noted above, even a single close Prometheus encounter adds only a few times 10^{-4} to the eccentricity, so particles are not, for example, ejected to Saturn (see also Sfair et al. 2009, Winter et al. 2010). The initial region here is, to be sure, narrower than in the other two cases (80 km *vs* 120 km) and this alone, on top of the high effective diffusion coefficient, may account for the strong depletion in process.

The diffusion is not unhindered though, because the stable radii at antiresonances (Lindblad resonances) are "sticky". Particles at these radii have very low RMS semimajor axis deviations and, in fact, perturbations are promptly cancelled so their behavior is not that of a diffusing particle at all. This is a plausible explanation for the spiky, non-Gaussian core of the 2008 strand PDF of $(a_f - a_i)$ (figure 17); the other cases probably share this property but are less obvious because their wings are not as broad. The spikes in figures 18 - 20 lie at stable radii in this sense.

Note furthermore in figures 18 - 20 that the stable zones in the three regions behave differently. In the 2008 strand region, particle densities are decreasing everywhere, but most stable zones persist at higher densities at both 10000 and 15000 Prometheus orbits (lower panel of figure 20). In the intermediate region, the overall density is not decreasing much throughout, but (especially visible in the lower panel) it seems that the stable zones blur and fade away going from 10000 to 20000 Prometheus orbits. The weakened stability in this region is perhaps due to the increasing relevance of Pandora, and manifested in the shallower low-RMS zones (figure 14). However, in the F core region, the stable zones are *growing* in density as time goes on (red *vs* black curves). This attests to their ability to increasingly capture diffusing particles from surrounding regions. It is the "stickiness" of stable regions that gives the PDFs of figure 17 their narrow, non-Gaussian cores.

This possibility is supported by **figure 21**. Here each test particle is plotted at its initial semimajor axis and its *mean* semimajor axis. The particles are colored red if their RMS semimajor axis deviation is less than 2 km (in the sense of figures 14 - 16). The upper and lower plots, for 10000 and 20000 Prometheus orbits respectively, have the same axes. The black points (moderate to high RMS particles) disperse radially as time goes on (there is a wider range of initial a for each average a), and moreover, their density seems to have decreased. This corresponds to the overall lower "background" level seen in figure 19. However, the *stable regions* (vertical bands of red points) seem more populous (this is confirmed quantitatively in figure 19). Moreover, after 20000 Prometheus orbits, low-RMS stable regions (red points) contain particles which started the evolution at a wider range of remote locations than they contain at 10000 orbits (top panel). This means that the stable regions are "attractors" for randomly diffusing particles. If a wandering particle chances to end up at a stable semimajor axis, it probably stays there. The combination of figures 19 and 21 suggests that, even while many or even most particles are chaotically perturbed into a diffusional evolution away from their initial location, there are very narrow, very stable zones *in the region of the F Ring core*, but *not in regions to either side* that can retain, and even collect, material over long times. We believe that the observed F Ring core lies in one such region.

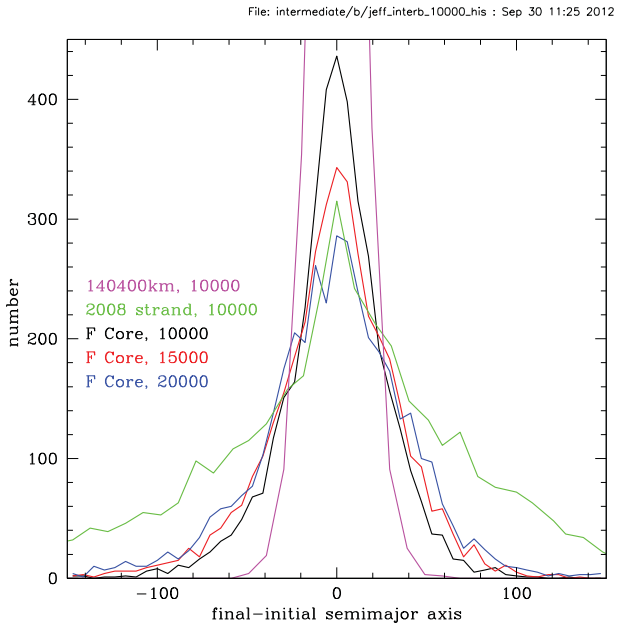

Figure 17: Probability distribution function (PDF) histogram for the difference $a_{\rm final} - a_{\rm initial}$ for all particles in each run, for various regions and run durations. The narrowest distribution, showing the smallest tendency for radial diffusion, in in the intermediate region. The broadest, showing the maximum diffusion rate after only 10000 Prometheus orbits, is for the 2008 strand region. Note, however, that the 2008 strand PDF is distinctly non-Gaussian and has a peak at small deviations (see section 3.4). For the F Ring core region, ongoing diffusion is evident in the growing width of the PDF with time.

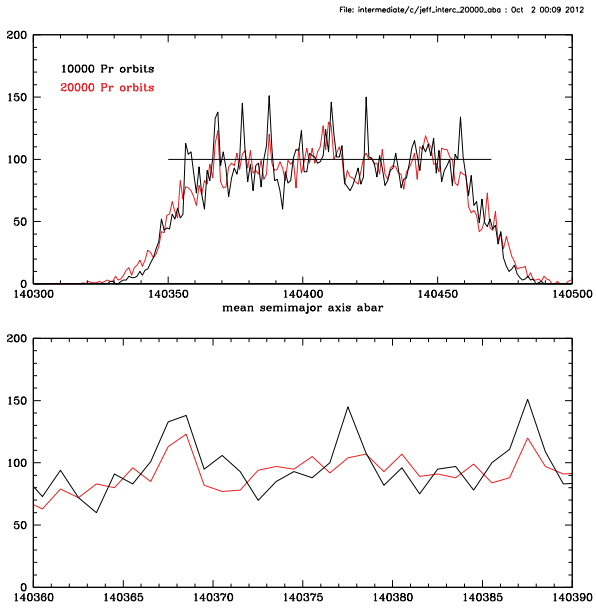

Figure 18: Histogram binning of all particles by average semimajor axis, in bins 1 km wide (here for the intermediate region). Upper and lower panels are simply at different radial scales. The black curve is after 10000 Prometheus orbits, and the red curve is after 20000 Prometheus orbits. The horizontal line indicates the radial width and number of particles per bin for the initial distribution, reflecting their nominal 10 m spacing. While little loss of particles from, at least, the central part of the zone can be seen, the stable zones evident at 10000 orbits have become washed out by 20000 orbits. See section 3.4.

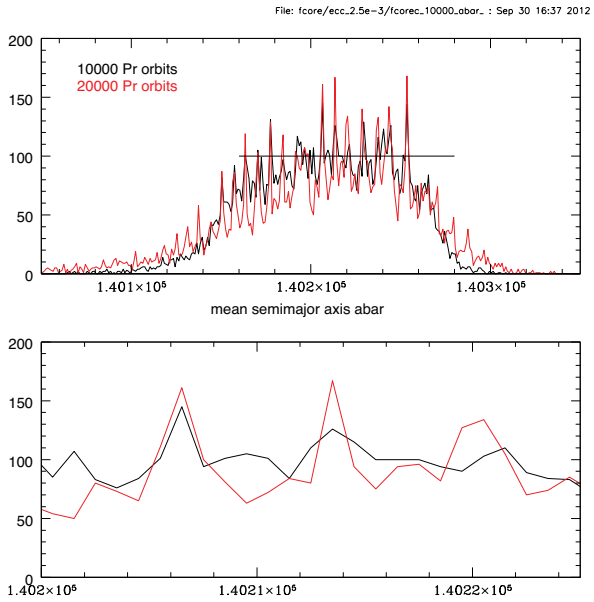

Figure 19: As in figure 18, but here for the F Ring core region. More loss of particles from the initial annulus is seen (especially away from stable zones), due to more rapid diffusion, but the stable zones actually grow in particle density from their initial values to 10000 orbits, and continue to gain particles between 10000 and 20000 Prometheus orbits. See section 3.4.

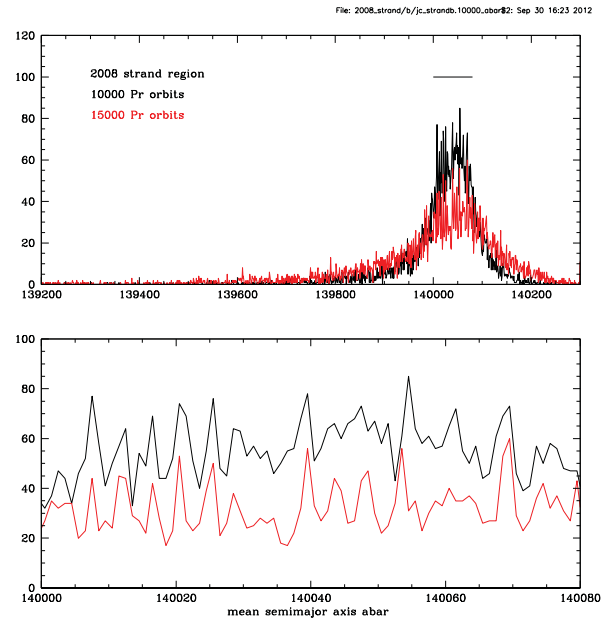

Figure 20: As in figure 18, but here for the 2008 strand region. Here the red curve is for 15000 orbits, however. Rapid and significant loss of particles from the entire region is seen, due to very rapid diffusion, even while some relatively stable zones continue to be evident. See section 3.4.

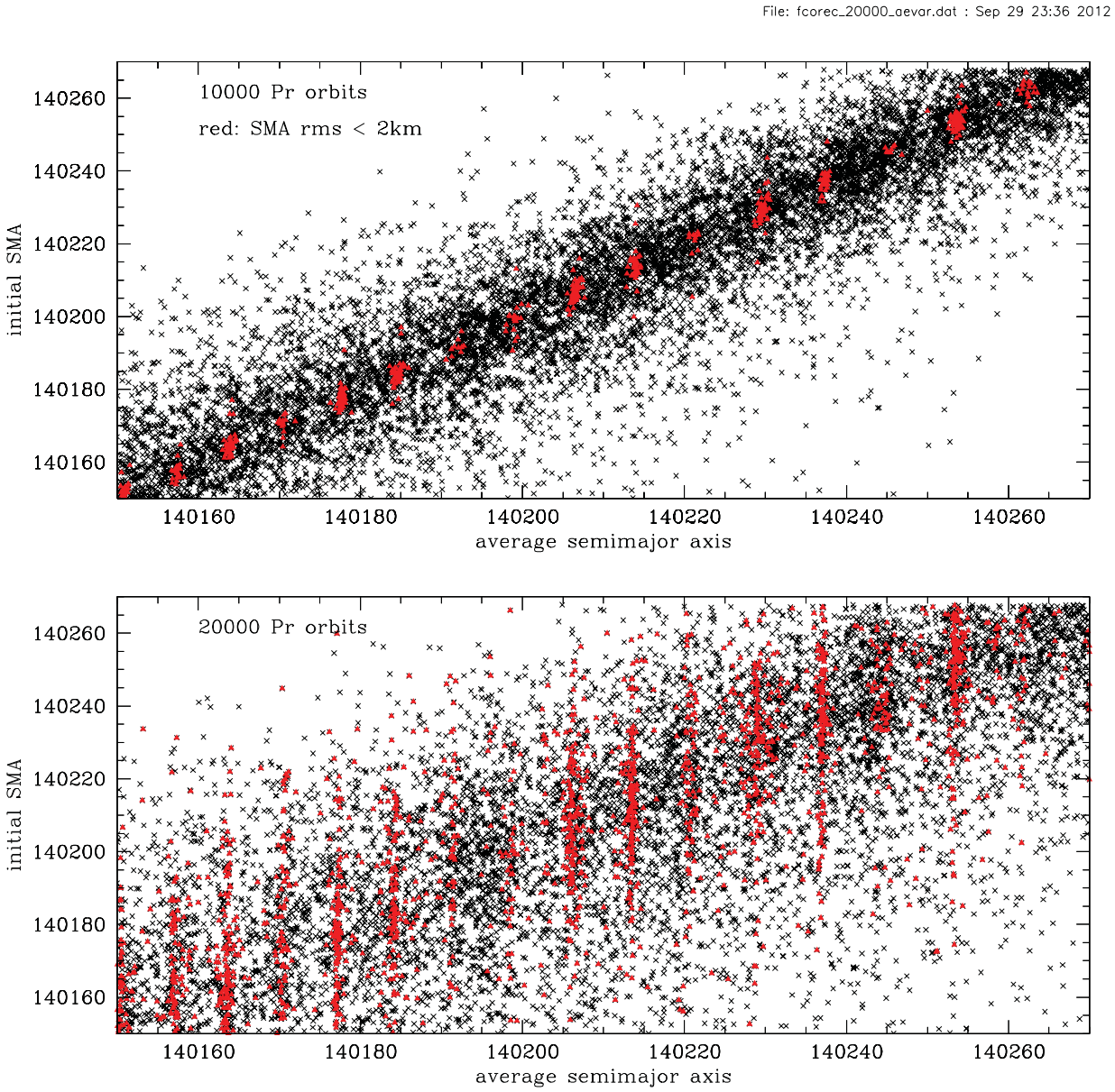

Figure 21: For the F Ring core region run, all 12000 particles are plotted according to their initial and average semimajor axis at 10000 Prometheus orbits (top) and 20000 orbits (bottom). Red particles (in the online version) are those with semimajor axis RMS less than 2 km; as seen before, these are found only at certain stable semimajor axes. Even at 10000 orbits, it can be seen that particles in a given stable zone originated over a range of initial a. This becomes even more obvious after 20000 Prometheus orbits, by which time stable zones have gained particles which started more than 40 km away and thus had to skip over several other stable zones. The apparent increase in number of particles per stable zone is shown quantitatively in figure 19. In this sense the grid of stable "antiresonances" is an attractor for particles. See section 3.4.

4 Discussion

Dermott (1981) first suggested that a single resonance might be responsible for the F Ring's structure, but that suggestion predated any knowledge of the eccentricities or orbits of the F Ring, Prometheus, or Pandora, assumed torque balance overall, and did not account for the period changes that ensue from mutual encounters on eccentric orbits. Since then, other hypotheses were put forward for creation and/or confinement of narrow, eccentric ringlets, notably by Hänninen and Salo (1994, 1995) and Goldreich et al. (1995). Both of these papers were couched in terms of low-order inner Lindblad resonances, but both should be applicable, with slight modifications, to high-order outer Lindblad resonances. They avoid the SB82 paradox of the F Ring not being in torque balance between straddling shepherds in the classical fashion, because they involve a single resonance. The resonance perturbs ring material into eccentric orbits by transferring energy and angular momentum to the ringlet as inappropriate rates for it to remain circular. Meanwhile the perturbation leads to reversal of the Keplerian (outward) flux of angular momentum in viscous systems, which keeps the ringlet from spreading radially in the expected way, as first described by the streamline deformation physics of Borderies et al. (1983, 1985). Hänninen and Salo (1994) note that the outcome of simulations like this is sensitively dependent on the mass of the perturber and the elasticity of interparticle collisions, as they affect the rate of energy dissipation; in some simulations the result is not a ringlet but a clear gap. Moreover, it is unclear whether the ultra-narrow F Ring can maintain the required radial gradients of eccentricity and/or apse longitude for the process to operate. While some influence of this sort might be operating in the actual F Ring, and it might indeed be a useful part of the full solution in helping collapse all the particles toward the same apse longitude, this appears to be rather different physics than the mechanism we propose here. In the model presented here, the narrowness of the stable structures we have found experimentally and motivated analytically has nothing to do with angular momentum flux reversal or viscosity (our simulations are collisionless) but only with the fact that particles *not* lying in such a narrow range will continue to diffuse until they *do*, with (so far unmodeled) collisional damping possibly playing a role in accomplishing this.

Determination of "the" F Ring core semimajor axis is complicated by the strong, widespread, and time-dependent Prometheus perturbations to the local radius of the core material. Analyses by Bosh et al. (2002) and subsequent workers (Murray et al. 2011, Marouf et al. 2011, Albers et al. 2012, and Cooper et al. 2012) differ at the several km level, ranging from 140219 km - 140223 km, and moreover show typical radial residuals of several km from the mean solution, far larger than the basic instrumental measurement precision, and no doubt caused by actual, local, and time dependent variations in the radius of material being sampled. Note that, even in our toy model, material rarely if ever actually *has* the "average" semimajor axis, but more realistically toggles back and forth across it on subsequent Prometheus encounters, or in some cases over a several-synodic-period-long cycle.

The most recent exhaustive analyses, using the largest amount of well-characterized data, are by Albers et al. (2012) and Cooper et al. (2012). Cooper et al. have the great advantage of multi-image, nearly instantaneous "snapshots" of an entire orbit, but the images are unfortunately all targeted very close to Prometheus, where the ring material is most likely to be disturbed. By excluding the most perturbed regions from their analysis, Cooper et al. arrive at a three-year average value of $a = 140220.8 \pm 0.3$ km, whereas Albers et al. (2012) use nearly 100 Cassini and Voyager occultations; their preferred result is $a = 140221.3 \pm 1.8$ km. The average of the Cooper et al. (2012) and Albers et al. (2012) results is thus close to 140221 km, with an uncertainty of perhaps 1 km. This average is indicated by the vertical dotted line in the lower panel of **figure 15**; it lies in excellent agreement with the semimajor axis of a prominent antiresonance or stable zone. The nearest alternates are 8.5 km away on either side, well out of the current uncertainties. It is interesting that the apparently favored

stable zone is affected by - and indeed biased towards - a (much weaker) Pandora resonance, and is perhaps for that reason slightly broader and less deep than the deepest (but narrowest) stable zones at "cleaner", more isolated Prometheus resonances. Nevertheless, the agreement shown is encouraging. Going into more accuracy at the present time regarding the exact resonance assignment of this stable zone is premature, because there are several different resonances (including corotation inclination and corotation eccentric resonances) within a km or so of the Lindblad resonance shown (see Goldreich and Tremaine 1980, Foryta and Sicardy 1996, and Murray and Dermott 1999 for instance). Further work will be needed to ascertain just which of this set of resonances is or are most directly responsible. A combination of Corotation and Lindblad resonances at this location might be the answer, along the lines of Neptune's ring arcs (Goldreich et al. 1986, Porco 1991, Sicardy 1991). These subtleties are being addressed in our ongoing work.

Nevertheless, the physics of the "antiresonances" described theoretically and shown numerically here does seem to offer an attractive explanation for the long-term stability of the F Ring core in the midst of what is essentially a chaotic region, wherein the ensemble eccentricity of large objects is expected to be pumped to several times 10^{-3} in a timescale of perhaps 10^3 years by cumulative encounters with Prometheus and the randomizing effects of Pandora and perhaps other moons. In a characteristic diffusion time of $10^2 - 10^3$ years, objects not fortunate enough to land in a stable zone will diffuse over $10^2 - 10^3$ km in semimajor axis. The diffusion is, however, impeded by some probability that particles will settle into a stable zone. As shown in figure 21, this is a fairly robust process at and near the location of the F Ring core. The presence of some pre-existing material, able to provide collisional damping, can only aid this trapping process. The stable zones have the nature of attractors in this chaotic environment.

The ensemble eccentricity advocated by CB88 for their putative moonlet belt (that resulting from a single Prometheus encounter) is clearly too small; however, this model was developed to explain the F Ring as a random, transient feature because of the problems in traditional shepherding models. This problem may now be moot; it seems there is a mechanism for preserving a narrow core of material at certain special semimajor axes for long periods of time. The microsignatures analyzed by CB88, which they interpreted as resulting from collisions between distinct members of a wide moonlet belt, might be the result of transient clumps and strands resulting from collisions between a smaller number of moonlets and the F Ring core itself, such as the 2008 event or the spiral strands analyzed by Charnoz et al. (2005).

Furthermore, Attree et al. (2012) note that low observed velocities in "mini-jets" are appropriate for single-encounter velocity perturbations only, and argue for damping on an encounter timescale. But damping is slow for large things. Neither we nor Attree et al. (2012) have attempted to estimate a damping timescale; it would depend on the mass of the objects to be damped, which could each be 10^{15} times more massive than typical F Ring particles. On the other hand, if the F Ring core does lie in an antiresonance, "prompt cancellation" can itself explain the low relative velocities. Similarly, if the AR enforces a very narrow ring core, differential precession is drastically slower and easier to offset by gentle collisional effects; it may even be that the constant and repetitive offsetting impulses have an effect on resetting the apse longitude.

We emphasize, however, that nothing in our simulations or the limited physics of our toy analytical model suggests a way of *aligning* the apse longitudes of all the material in the F Ring core, even once it all lies at an antiresonance. This might be a byproduct of damping, which can have the effect of driving collisionally interacting material into a common orbit. We are pursuing this aspect of the problem in current work. Another interesting question is just how unique the current stable zone might be. There are a number of (apparently) comparably stable locations in the region; is the presence of a *single* F Ring in this specific one accidental? Is it a coincidence that this one seems extremely close

to the magic criterion $(m\dot{\omega}/n_o) = 1/2$ (equation 19)? Maybe the initial disruption/creation event left a rubble strand that was too narrow to cover several candidate stable zones. Or, even if several strands formed from an initially broader rubble band in adjacent stable zones, these other strands might just all be swallowed up by the mass-and-area dominant strand subsequent to differential precession and dissipative collisions. The eccentricity of such a dominant strand or core might have grown with time, due to whatever physics now excites it, until at its current eccentricity, the precessing core would interact with similar, independently precessing stable zones over a region 700km wide, covering all three zones studied in this paper (see figure **??**).

Regarding the 2008 strand, our simulations show that particles in this semimajor axis range disperse at a high rate, consistent with its disappearance over five years (C. Murray, personal communication 2012). This is because it is so close to Prometheus that highly nonlinear perturbations are much harder to "cancel promptly" on successive encounters, and period changes make it very hard to correlate true anomalies from one encounter to the next. Even then, throughout 15000 Prometheus orbits, our simulations show that certain special semimajor axes remain more stable and populated than others. It would be profitable to explore the limited dataset to see if there is any evidence that long-lasting particles did indeed reside at any of the preferred locations.

4.1 Speculation on a self-perpetuating process for F Ring activity and production of 2004S6-like objects

One might speculate on a way that 2004S6-like objects might be produced repeatedly, in a self-perpetuating way, given only that at some time some of them did exist (such as perhaps at the time of initial formation of the F Ring from some large disruptive event). When such an object has an unusually violent collision with, perhaps, an unusually large member of, or dense part of, the F Ring core, a giant strand like that seen in 2008 may result, spraying material over hundreds of km in radius and semimajor axis. Such a clump might have been what McGhee et al. (2001) observed in 1995-1996. Such clumps cannot be produced by collisions *between* F Ring core members, because their relative velocities are too low (Attree et al. 2012). Material in such a strand rapidly disperses due to chaotic perturbations *unless* it lies at one of the several stable zones it overlaps. Material fortunate enough to end up in one of these zones may be able to persist long enough for the "attractor" nature of the stable zone, perhaps augmented by self-gravity, to form a finite number of massive objects, perhaps of km size. A train of such objects can be seen at the same distance from Saturn in the longest-lived remnant of the F Ring strand (Murray et al 2011); because their motion was not tracked over an entire orbit however, their semimajor axis is not known. However, even these objects are not able to survive forever and eventually chaotic perturbations pump their eccentricities back to several times 10^{-3}, allowing them to re-cross and encounter the F Ring, essentially becoming reincarnations of 2004S6. This cycle might be initiated by apse antialignment, perhaps settling down before the subsequent antialignment, and moreover, it might take several years to unfold because the collision probability of a random newly formed moonlet with a dense part of the F Ring core might be fairly small, per crossing, depending on node and apse locations and the patchy nature of the core itself (Marouf et al. 2011).

5 Conclusions and future work

We have found numerically, and explained analytically, many narrow radial zones in the F Ring region, within which particle semimajor axes can remain essentially constant for long periods of time

because Prometheus perturbations at one encounter are promptly cancelled at the next encounter. One of these stable radii corresponds closely to the observed semimajor axis of the F Ring core. Away from these stable radii, particles are chaotically perturbed and diffuse radially over hundreds of km on a timescale of $10^2 - 10^3$ years. The stable radii lie very close to, or at, Lindblad resonances and are activated only because of the unusual property that particle apse longitudes in this region precess by π over a synodic encounter period with Prometheus. The stable zones in the region where the F Ring core is found are demonstrably *more* stable than in regions only a few hundred km away, and in fact act as "attractors" for diffusing material (figures 15 and 21). The stable zone in which the actual F Ring core lies is not in any way particularly unique relative to its dozen or so nearest neighbors; in this sense we regard the *specific* location of the F Ring an accident in which some locally generated debris ended up in that particular site, rather than some nearby site. While helping us understand the location and narrowness of the F Ring core, the model does not explain why the F Ring core material all shares a common *apse longitude* and precesses as a unit; this aspect is currently under study.

6 Acknowledgements

This paper is the result of a study that started 22 years ago, but went into hibernation shortly after the Boulder DPS meeting (Scargle et al. 1993). Bob Hogan joined our group at the beginning of the project, and was responsible for initial development and testing, incorporating some input subroutines from several other coauthors, and then maintaining the N-body integration codes and their user interfaces across various computer platforms over more than a decade, which allowed the thread to be picked up again in 2008. Amongst the many other projects he worked on during that 20 years, Bob continued to contribute to this one until shortly before his death in February 2012; he would be happy to see it come to fruition. We also thank Nick Cooper, Martin Duncan, Dick French, Peter Goldreich, Bob Jacobson, Daniel Jontof-Hutter, Jack Lissauer, Essam Marouf, Carl Murray, Bruno Sicardy, and Matt Tiscareno for codes, extremely useful discussions, and provision of material prior to publication.

symbol	property	value or section
GM	Saturn's gravitational mass	3.79312077$\times 10^{22}$cm^3/s^2 (a)
R_S	Saturn's radius	60330 km
J_2, J_4, J_6	Saturn's gravitational harmonics	16290.71, -935.83, 86.14 (b)
n_s	mean motion of Prometheus	587.285237 deg/day (c)
M_s/M	Prometheus' mass / Saturn mass	2.75499$\times 10^{-10}$ (a)
$a, \overline{a}$	semimajor axis and its time average	Sections 2, 3
a_0, a_s	semimajor axis (particle and Prometheus)	Section 2
e_0, e_s	eccentricity (particle and Prometheus)	Section 2
n_0	mean motion of particle	Section 2
κ_0, κ_s	epicycle frequency (particle and Prometheus)	Section 2.2, fig. 6, App. A
P_0	particle period = $2\pi/n_0$	Section 2.1
P_{syn}	synodic period = $2\pi/\|n_0 - n_s\|$	Section 2.1
f, g, ω	mean anomaly, inertial and periapse longitudes; $f = g - \omega$	Section 2
Ψ	mean anomaly of particle in "merged" system of SB82	Section 2.2
$\phi = \omega^*$	periapse longitude of particle in "merged" system of SB82	Section 2.2
h, k	$h = e\sin f, k = e\cos f$	Section 2.1
l, m	integers describing orbital resonances	Section 2.1, Appendix A
r_L, r_C	semimajor axes at Lindblad and Corotational resonances	Appendix A
ϵ	fractional distance between resonances of order $m, m \pm 1$	Section 2.1
s	particle-perturber radial separation at encounter	Sections 2.1,2.2
R, T	radial and transverse forces on particle at encounter	Sections 2.1,2.2; fig. 3
$\mathcal{D}$	effective diffusion coefficient in chaotic region	Section 3.4

Table 1: (a) R. A. Jacobson, Cassini state vectors; personal communication 2008; (b) all $\times 10^{-6}$ (from (a); see Appendix B); (c) Jacobson et al (2008); also for Pandora, n=572.788589 deg/day

Appendix A: Resonances

The basic tools for calculating the locations and strengths of inner and outer, first and higher order, Lindblad and Corotation resonances are provided by Goldreich and Tremaine (1979, 1980; henceforth GT79 and GT80). Lissauer and Cuzzi (1982; henceforth LC82) approximated some of these expressions and applied them to inner Lindlad resonances (ILR). Here we generalize the approach to outer Lindblad (OLR) and inner and outer corotation resonances (ICR, OCR). The notation is that of GT80 and we will not repeat all the equations presented therein.

The gravitational potential ϕ^s of a perturber s, with semimajor axis a_s, orbital frequency $n(a_s) = n_s$, and epicycle frequency $\kappa(a_s) = \kappa_s$ can be Fourier expanded in terms of $\phi^s_{l,m}$, its Fourier harmonics with integer indices (l, m) (here $m > 0$); the *pattern speed* or angular frequency of this potential field is $n_{l,m}$.

Lindblad resonances of order $(l : m - 1)$ are found at semimajor axes r_L where $n(r_L) \pm \kappa(r_L)/m = m_{l,m}$; here the plus sign defines Outer Lindblad Resonances (OLRs) and the minus sign defines Inner Lindblad Resonances (ILRs). First-order resonances involve $l = m$ and the pattern speed is simply the perturber orbit frequency. Corotation resonances (CR) are defined by $n(r_C) = n_{l,m}$. All first-order CR are degenerate at a_s where $n_{l,m} = n_s$, making them of no interest here. Second-order resonances ($l = m \pm 1$) result in pattern speeds offset from the perturber's orbit frequency. Each of these patterns has its own ILR, CR, and OLR; the OLR (ILR) associated with

a second-order inner (Outer) CR lies at the perturber's orbit (like all the first-order CR) so these are also of no interest to us. The second-order ILR (OLR) of interest are associated with the inner (outer) CR which obey $l - m = 1$ ($l - m = -1$), respectively. Figure 1 of GT80 shows the combinations of interest for first- and second-order resonances. Resonances are denoted by their value of m which corresponds to the number of lobes in the corotating potential at the position of the perturbed particle.

This discussion is restricted to resonances where the eccentricity of the perturber is much larger than that of the test particle, which is generally fine for ring studies but not necessarily valid for the F Ring region. When test particles become as eccentric as the perturbing moonlets, new resonances arise related to the test particles' periods, masses, and eccentricities, at slightly different locations, and the situation becomes more complex (GT80, Foryta and Sicardy 1996). We will neglect these latter resonances in our initial survey of resonances in the F ring region, restricting ourselves to those involving the period and eccentricity of the perturber. However it should be kept in mind that this situation makes the dynamics of test particles more chaotic than might be obvious from the web of resonances we calculate and display.

Our resonance locations are calculated iteratively at first and second order from the basic definitions of Lindblad and Corotation resonances (GT80, LC82), defined where the local mean motion n or epicycle frequency κ is equal to some angular pattern speed $n_{l,m}$, where following GT80 the pattern speed (for eccentric resonances) is:

$$n_{l,m} = n_s + \left(\frac{l-m}{m}\right)\kappa_s \tag{20}$$

where n_s and κ_s are the mean motion and epicycle frequency of the perturber, (l, m) are integers, and the perturber's semimajor axis is r_s. First order resonances correspond to $l = m$ and second order to $l = m + 1$. Then for Lindblad resonances (GT80),

$$\kappa(r_L) = \pm m(n_{l,m} - n(r_L)) \tag{21}$$

and for corotation resonances

$$n(r_C) = n_{l,m}. \tag{22}$$

For vertical or inclination resonances the vertical frequency μ replaces the epicycle frequency κ in the equations above.

We use Newton's method to determine the values of r_L (and in general r_C) that satisfy these equations, adopting standard values for Saturn's mass and gravitational harmonics (Table 1). We initialize the properties of the perturbing moon in terms of its angular frequency or mean motion n_s, which is easily and accurately measured, determining its semimajor axis iteratively in the potential field of an oblate planet using Newton's method. The planet's oblateness is characterized by J_2, J_4, and J_6. The difference in quoted mean motion between Jacobson et al. (2008) and French et al. (2003) should make a difference at the sub-km level; the Jacobson et al. (2008) mean motion actually returns the French et al. (2003) semimajor axis to this level of accuracy.

The strength of each resonance will be taken as its torque per unit surface mass density $T_{l,m}/\sigma$, given for Lindblad and corotational resonances by equations (13) and (14) of GT80, where $T_{l,m}/\sigma$ can be related to other useful parameters such as the effective resonance width (see LC82). We use these torques merely to get a sense of which are the most important in a relative sense, and will present their absolute values (actually ILR and CR torques are negative, and OLR torques are positive). These torques are expressed for each resonance order l, m in terms of the perturber's frequencies $n_s, \kappa_s, n_{l,m}$, the test particle's frequencies $n(a), \kappa(a)$, and the perturbing potential $\phi^s_{l,m}$ (GT80, eqns 7-9) and its radial derivative. The potential $\phi^s_{l,m}$ and its radial derivative are in turn expressed in terms of Laplace

coefficients for order m (GT80, eqn 10; Brouwer and Clemence 1961, p. 494ff) which depend on the semimajor axes of the perturber and the test particles (at each resonance), and can be evaluated either by brute force (GT80 eqn 10) or iteratively. Brouwer and Clemence (1961) present recursion relations which only converge for $a_s > a$ (inner resonances), stating merely that the situation is more complicated when $a_s < a$ (as for OLR and OCR). We have used a code kindly provided by M. Tiscareno, built upon an earlier version developed by R. Malhotra and P. Nicholson, which uses the Brouwer and Clemence recursion scheme and swaps the roles of a and a_s to obtain the Laplace coefficients when $a_s < a$. We tested this approach against brute force integration of equation 10 of GT 80. The complete expression leads to a quite small inner/outer asymmetry in the coefficients (at the few percent level) for the same radial separation. For the high orders of interest here ($m \sim 100$), inner and outer resonances of the same order are at nearly the same distance from the perturber. The small asymmetry arises because, for some radial difference Δ, $r/a_s = 1 - \Delta/a_s$ for inner resonances, but $a_s/r = 1 - \Delta/a_s$+ higher order terms for outer resonances. For our purposes the recursive relation, with the symmetry assumption, is accurate to less than a percent, and is more than adequate for our purposes. With current computers, the Laplace coefficients and their derivatives are not hard to evaluate by direct integration for tasks where higher accuracy is needed.

We checked our resonance locations and strengths against tables in LC82, adopting their planet and satellite parameters (note there is a typo in the units of GM_S in LC82 table 1; the units should be m^3sec^{-2}. We also then checked our results against an independent code of M. Tiscareno (personal communication 2009, which, of course, contains the same Laplace coefficient expressions). For the most up to date orbit parameters and masses of the ringmoons Prometheus, Pandora, Janus, and Epimetheus we relied on Jacobson et al. (2008; tables 5 and 8).

The second-order inclination and eccentricity corotation resonances of order m are located very close to first-order Lindblad resonances of order $m - 1$, and distinguishing them is operationally subtle (Goldreich et al. 1986; Foryta and Sicardy 1996). Thus the F Ring core might turn out to be less physically due to a Lindblad resonance, as discussed herein, than to a corresponding corotational resonance very near by. For the purpose of this paper we will not discuss corotational resonances in any detail, but we are are pursuing this subject and will address it in a subsequent paper.

Appendix B: Code numerics

Our basic code is a Bulirsch-Stoer integrator (Stoer and Bulirsch 1980), and in particular the variant due to Gear (1971). It is not the fastest code available but is extremely accurate and reliable, suitable for systems with near-chaotic conditions. We wanted to be sure to avoid numerically generated "false chaos" (Duncan et al. 1989). The BS integrator dynamically changes the integration timestep to maintain a stipulated precision; in close-encounter geometries the timestep gets very small and automatically grows when forces are changing less rapidly. The integration is done in Cartesian geometry, in the center-of-mass system; but for analysis and interpretation, the state vectors (co-ordinates and velocities) are converted into osculating "epicyclic" orbital elements suitable for describing orbits about an oblate primary, as described by Borderies-Rappaport and Longaretti (1994). These are analogous to the classical Keplerian orbital elements a, e, i, *etc.*; but unlike the latter, the epicyclic elements do not undergo short-period oscillations due to the primary's dynamical oblateness. We used a variety of codes to convert between state vectors and epicyclic elements, some by Martin Duncan with Hal Levison and Luke Dones, based on Fitzpatrick's Priciples of Celestial Mechanics, and others by Mark Showalter or Tony Dobrovolskis, based on Borderies-Rappaport and Longaretti (1994). Our conversion codes are accurate to first degree in e and i, but exact in the oblateness coefficients J_2, J_4,

and J_6.

For the Cartesian integrations, the accuracy parameter is set at 10^{-14}; going from 10^{-14} to 10^{-12} led to artificial chaos or premature divergence in 3/4 of orbits inspected within 1000 Prometheus orbits. However, going to an accuracy parameter less than 10^{-14} became prohibitive in cpu time. Individual runs with 4000 massless particles and 14 massive perturbers can typically complete 10000 Prometheus orbits in 15 cpu hours on a Mac laptop. The binary state files we use to restart the code are cumulative, and can become cumbersome (tens of GB) after more than 20000 Prometheus orbits for this number of particles, because coordinates and velocities are stored for each particle on each orbit.

The code computes the gravitational forces on massless test particles from Atlas, Prometheus, Pandora, Janus, Epimetheus, Mimas, Enceladus, Tethys, Dione, Rhea, Titan, Hyperion, Iapetus and Phoebe (!). The initial positions and velocities of these bodies was provided in a state file for 01/02/2004, kindly provided by Bob Jacobson. An example of the output, for Prometheus and Pandora, is shown in **figure 22**. The form of the potential and its relation to mean motion and epicycle frequency we have used is

$$n^2 = \left(\frac{GM}{a^3}\right)\left(1 + \frac{3}{2}J_2\left(\frac{R_S}{a}\right)^2 - \frac{9}{16}J_4\left(\frac{R_S}{a}\right)^4 - \frac{15}{8}J_6\left(\frac{R_S}{a}\right)^6\right) \tag{23}$$

$$\kappa^2 = \left(\frac{GM}{a^3}\right)\left(1 - \frac{3}{2}J_2\left(\frac{R_S}{a}\right)^2 + \frac{45}{8}J_4\left(\frac{R_S}{a}\right)^4 - \frac{175}{16}J_6\left(\frac{R_S}{a}\right)^6\right); \tag{24}$$

Using these constants and relations, our code gives a starting semimajor axis for Prometheus of 139377km, in very good agreement with the high-precision results of French et al. (2003) averaged over three years, and consistent with the value quoted by Jacobson et al. (2008) which is apparently rounded to the nearest 10km. As figure 22 shows, semimajor axes and thus the resonances and stable zones tied to them move around at a larger amplitude than 0.1km in any case, due to chaotic influences of Prometheus and Pandora on each other. Our stable zones persist in the face of this small variability.

References

Albers, N.; Sremčević, M.; Colwell, J. E.; Esposito, L. W. (2012) Saturn's F ring as seen by Cassini UVIS: Kinematics and statistics; Icarus, 217, 367-388

Attree, N. O.; Murray, C. D.; Cooper, N. J.; Williams, G. A. (2012) Detection of Low-velocity Collisions in Saturn's F Ring; Astrophysical Journal, 755, L27-L31.

Beurle, K.; Murray, C. D.; Williams, G. A.; Evans, M. W.; Cooper, N. J.; Agnor, C. B. (2010) Direct Evidence for Gravitational Instability and Moonlet Formation in Saturn's Rings; Astrophysical Journal, 718, L176-L180

Borderies-Rappaport, N., and P.-Y. Longaretti (1994) Test particle motion around an oblate planet. Icarus, 107, 129-141.

Bosh, A. S.; Olkin, C. B.; French, R. G.; Nicholson, P. D. (2002) Saturn's F Ring: Kinematics and Particle Sizes from Stellar Occultation Studies; Icarus, 157, 57-75

Brouwer, D.; Clemence, G. M. (1961) Methods of celestial mechanics; New York: Academic Press, 1961

Burns, J. A. (1976) Elementary Derivation of the perturbation equations of celestial mechanics; Am. Jnl. Physics 44, 944-949; Erratum: Am. J. Phys. 45, 1230.

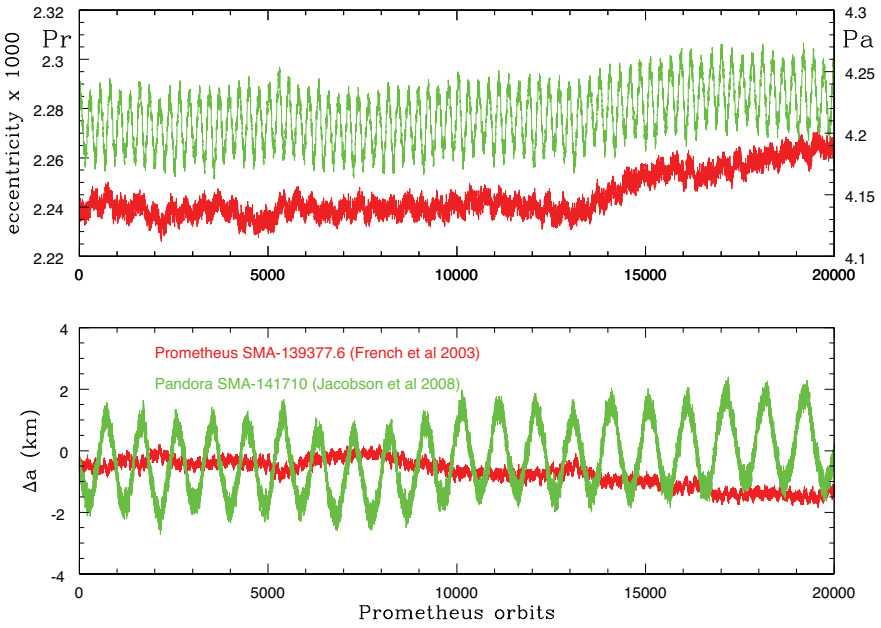

Figure 22: Long timescale evolution of Prometheus (red) and Pandora (green); compare, for instance, with French et al. 2003. A greyscale version will be provided for the print version.

Charnoz, S.; Porco, C. C.; Déau, E.; Brahic, A.; Spitale, J. N.; Bacques, G.; Baillie, K. (2005) Cassini Discovers a Kinematic Spiral Ring Around Saturn; Science, 310, 1300-1304

Chavez, C. E. (2009) Appearance of Saturns F ring azimuthal channels for the anti-alignment configuration between the ring and Prometheus; Icarus, 203, 233-237

Colwell, J. E.; Nicholson, P. D.; Tiscareno, M. S.; Murray, C. D.; French, R. G.; Marouf, E. A. (2009) The Structure of Saturn's Rings; in "Saturn from Cassini-Huygens", ed. Dougherty, Michele K.; Esposito, Larry W.; Krimigis, Stamatios M., ISBN 978-1-4020-9216-9. Springer Science+Business Media B.V.; 375-412

Cooper, N. J., C. D. Murray, and G. A. Williams (2012) Local Variability in the Orbit of Saturns F Ring; submitted to Astronomical Journal

Cuzzi, J. N.; Burns, J. A. (1988) Charged particle depletion surrounding Saturn's F ring - Evidence for a moonlet belt? Icarus, 74, 284-324

Cuzzi, J. N. and J. D. Scargle (1985) Wavy edges suggest moonlet in Encke's gap; Astrophys. J., 292, 276-290

Danby, J. M. A. (1962) Fundamentals of Celestial mechanics; MacMillan, N.Y.

Dermott, S. F. (1981) The 'braided' F Ring of Saturn; Nature, 290, 454-457

Dermott, S. F. (1984) Dynamics of narrow rings; in "Planetary rings" Tucson, AZ, University of Arizona Press, 589-637.

Duncan, M.; Quinn, T.; Tremaine, S. (1989) The long-term evolution of orbits in the solar system - A mapping approach; Icarus 82, 402-418

Foryta, D. W.; Sicardy, B.(1996) The Dynamics of the Neptunian Adams Ring's Arcs; Icarus 123, 129-167

French, R. G.; McGhee, C. A.; Dones, L.; Lissauer, J. J. (2003) Saturn's wayward shepherds: the peregrinations of Prometheus and Pandora; Icarus 162, 143-170.

French, R.S.; Showalter, M. R.; Sfair, R.; Argelles, C. A.; Pajuelo, M.; Becerra, P.; Hedman, M. M.; Nicholson, P. D. (2012) The brightening of Saturn's F ring; Icarus, 219, 181-193.

Gear, C.W. 1971, Numerical Initial Value Problems in Ordinary Differential Equations (Englewood Cliffs, NJ: Prentice-Hall), 6.1.4.

Goldreich, P.; Rappaport, N.; Sicardy, B. (1995) Single sided shepherding. Icarus 118, 414-417

Goldreich, P.; Tremaine, S. (1979) Towards a theory for the Uranian rings; Nature, 277, 97-99.

Goldreich, P.; Tremaine, S. (1980) Disk-satellite interactions; Astrophys. J. 241, 425-441

Goldreich, P.; Tremaine, S.; Borderies, N. (1986) Towards a theory for Neptune's arc rings; Astron. J. 92, 490-494

Hänninen, J.; Salo, H. (1994) Collisional simulations of satellite Lindblad resonances. 2: Formation of narrow ringlets; Icarus, 108, 325-346

Hänninen, J.; Salo, H. (1995) Formation of isolated narrow ringlets by a single satellite. Icarus 117, 435-438

Henon, M.; Petit, J.-M. (1986) Series expansion for encounter-type solutions of Hill's problem; Celest. Mech. 38, 67-100.

Jacobson, R. A., J. Spitale, C. C. Porco, K. Beurle, N. J. Cooper, M. W. Evans, and C. D. Murray (2008) Revised orbits of Saturn's small inner satellites; Astron. J. 135, 261263

Lissauer, J. J.; Cuzzi, J. N. (1982) Resonances in Saturn's rings; Astron. J., 87, 1051-1058.

McGhee, C. A.; Nicholson, P. D.; French, R. G.; Hall, K. J. (2001) HST Observations of Saturnian Satellites during the 1995 Ring Plane Crossings; Icarus, 152, 282-315

Marouf, E., K. Wong, R. French, N. Rappaport, and C. McGhee(2010), The Discontinuous Core of Saturn's F-Ring and Orbit Model. Abstract 22.02, BAAS volume 42, #4 (42nd DPS Meetings, Pasadena, CA, October 3-8).

Meinke, B. K.; Esposito, L. W.; Albers, N.; Sremčević, M. (2012) Classification of F ring features observed in Cassini UVIS occultations; Icarus, 218, 545-554

Murray, C.D., N. Cooper, G.A. Williams, M.W. Evans, T. Wong (2011); Strands and Clumps in Saturns F ring. Paper presented at Cornell Rings Workshop, August 2011

Murray, C.D.; Chavez, C.; Beurle, K.; Cooper, N.; Evans, M. W.; Burns, J. A.; Porco, C. C. (2005) How Prometheus creates structure in Saturn's F ring; Nature, 437, 1326-1329

Murray, C.D.; Beurle, K.; Cooper, N. J.; Evans, M. W.; Williams, G. A.; Charnoz, S. (2008) The determination of the structure of Saturn's F ring by nearby moonlets; Nature, 453, 739-744

Murray, C. D. and S. F. Dermott (1999); Solar System Dynamics; Cambridge UNiversity Press, Cambridge, UK.

Petit, J.-M.; Henon, M. (1987) A numerical simulation of planetary rings. I - Binary encounters; Astron. Astrophys. 173, 389-404.

Porco, C. C. (1991) An explanation for Neptune's ring arcs; Science 253, 995-1001

Scargle, J.; Cuzzi, J.; Dobrovolskis, A.; Dones, L.; Hogan, R.; Levit, C.; Showalter, M.; Young, K. (1993) Dynamical Evolution of Saturn's Rings; 25th DPS Meeting, #26.04; B.A.A.S., 25, p.1103

Sfair, R.; Winter, S. M. Giuliatti; Mourão, D. C.; Winter, O. C. (2009) Dynamical evolution of Saturn's F ring dust particles; M.N.R.A.S. 395, 2157-2161

Showalter, M. R.; Burns, J. A. (1982) A numerical study of Saturn's F-ring; Icarus, 52, 526-544.

Showalter, M. R.; Pollack, J. B.; Ockert, M. E.; Doyle, L. R.; Dalton, J. B. (1992) A photometric study of Saturn's F Ring; Icarus, 100, 394-411

Sicardy, B. (1991) Numerical exploration of planetary arc dynamics; Icarus 89, 197-219.

Stoer, J., and Bulirsch, R. 1980, Introduction to Numerical Analysis (New York: Springer-Verlag), 7.2.12.

Winter, O. C.; Mourão, D. C.; Giuliatti Winter, S. M.; Spahn, F.; da Cruz, C. (2007) Moonlets wandering on a leash-ring; M.N.R.A.S. 380, L54-L57

Winter, O. C.; Mourão, D. C.; Giuliatti Winter, S. M. (2010) Short Lyapunov time: a method for identifying confined chaos Astron. Astrophys., 523,A67-A72.

Wisdom, J. (1983) Chaotic behavior and the origin of the 3/1 Kirkwood gap; Icarus, 56, 51-74.